Remodeling of adhesion and modulation of mechanical tensile forces during apoptosis in *Drosophila* epithelium

Xiang Teng[1,2], Lei Qin[2], Roland Le Borgne[3,4], Yusuke Toyama[1,2,5,*]

1 Department of Biological Sciences, National University of Singapore, Singapore
2 Mechanobiology Institute, National University of Singapore, Singapore
3 CNRS, UMR 6290, Institute of Genetics and Development of Rennes, Rennes, France
4 Université Rennes 1, Faculté de Médecine, Rennes, France
5 Temasek Life Sciences Laboratory, Singapore

* Author for correspondence (dbsty@nus.edu.sg).

Development • Advance article

Abstract

Apoptosis is a mechanism of eliminating damaged or unnecessary cells during development and tissue homeostasis. During apoptosis within a tissue, the adhesions between dying and neighboring non-dying cells need to be remodeled so that the apoptotic cell is expelled. In parallel, the contraction of actomyosin cables formed in apoptotic and neighboring cells drive cell extrusion. To date, the coordination between the dynamics of cell adhesion and the progressive changes in tissue tension around an apoptotic cell is not fully understood. Live imaging of histoblast expansion, which is a coordinated tissue replacement process during *Drosophila* metamorphosis, shows remodeling of adherens junctions (AJs) between apoptotic and non-dying cells, with a reduction in the levels of AJ components, including E-cadherin. Concurrently, surrounding tissue tension is transiently released. Contraction of a supra-cellular actomyosin cable, which forms in neighboring cells, brings neighboring cells together and further reshapes tissue tension toward the completion of extrusion. We propose a model according which modulation of tissue tension represents a mechanism of apoptotic cell extrusion, and would further influence biochemical signals of neighboring non-apoptotic cells.

Development • Advance article

Introduction

Throughout development and adult life, epithelia undergo constant growth and turnover. As a cell population changes, epithelial architecture needs to be maintained and this is done through the tight intercellular adhesions supported by adherens junctions (AJs) (Harris and Tepass, 2010, Takeichi, 2014, Lecuit and Yap, 2015). Apoptosis, or programmed cell death, is the most common mechanism of eliminating damaged or unnecessary cells during embryonic development, and tissue homeostasis (Jacobson et al., 1997). When cells within a tissue undergo apoptosis, the adhesions between the dying and neighboring non-dying cells need to be remodeled. This ensures the apoptotic cell can be expelled from a tissue without compromising tissue cohesion. The loss of adhesions in the apoptotic process has been studied, with a focus on the disruption of cell-cell junctions associated with caspase activation. Members of the caspase family serve as the key executors of apoptosis (Riedl and Shi, 2004, Miura, 2012). For instance, AJ components, such as E-cadherin (E-cad) and β-catenin (β-cat) are known substrates of caspase-3 in mammalian cells (Bannerman et al., 1998, Brancolini et al., 1997). In *Drosophila* the reduction in the levels of E-cad from AJs is associated with the cleavage of the β-cat homolog Armadillo by the *Drosophila* effector caspase DrICE (Kessler and Muller, 2009).

Along with AJ remodeling, the process of cell extrusion is also crucial in the expulsion of dying cells from a tissue. In tissue culture, apoptotic cells autonomously develop an actomyosin cable, and the neighboring non-apoptotic cells also form a supra-cellular actomyosin purse-string (Rosenblatt et al., 2001, Kuipers et al., 2014).

Development • Advance article

These cables exert contractile force and contribute to extrusion (Rosenblatt et al., 2001, Kuipers et al., 2014). Recently, it was shown that E-cad is critical in the transmission of contractile force to neighboring cells (Lubkov and Bar-Sagi, 2014), and in the recruitment of Coronin-1B, which aligns the actomyosin cable (Michael et al., 2016) during apoptotic cell extrusion. Together, these findings highlight an intriguing interplay between AJ dynamics and the cytoskeleton, and in turn, progressive changes in tissue tension around the apoptotic cell. The mechanisms resulting from this interplay remain to be fully understood.

We elected to study tissue replacement during histoblast expansion in *Drosophila*. At the onset of pupal development, the quiescent abdominal histoblasts (precursors of the adult epidermal cells) are grouped in nests embedded amongst larval epidermal cells (LECs) (Fig. 1a, Movie 1). As metamorphosis progresses, histoblasts exhibit rapid proliferation and active migration, leading to the growth and expansion of the nests (Ninov et al., 2007, Ninov et al., 2010). Concurrently, pre-existing LECs undergo caspase-3 mediated apoptosis (Nakajima et al., 2011). The majority of the apoptotic cells in *Drosophila,* including LECs, extrude basally. This is observed in, for example, embryonic tissue (Kiehart et al., 2000, Toyama et al., 2008, Meghana et al., 2011, Muliyil et al., 2011, Sokolow et al., 2012, Monier et al., 2015), larval tissue (Ninov et al., 2007), imaginal discs (Shen and Dahmann, 2005, Manjon et al., 2007, Monier et al., 2015), and adult tissue during pupa (Kuranaga et al., 2011, Marinari et al., 2012). This is intriguingly contrary to apical cell extrusion in most vertebrates (Rosenblatt et al., 2001, Eisenhoffer et al., 2012, Yamaguchi et al., 2011). Around 80%

Development • Advance article

of LECs undergo apoptosis in proximity to histoblast nests (hereafter referred to as 'boundary' LECs) and ~20% of LECs die away from the nests (hereafter referred to as 'non-boundary' LECs) (Ninov et al., 2007, Bischoff and Cseresnyes, 2009, Nakajima et al., 2011). Although the proliferation of histoblasts is known to contribute to histoblast expansion (Ninov et al., 2007, Ninov et al., 2010), it was not clear whether the mechanics of LEC apoptosis also contributes to the expansion (Ninov et al., 2007, Bischoff and Cseresnyes, 2009).

In this study, we reveal that during the extrusion of apoptotic LECs, AJs between apoptotic and neighboring cells become remodeled, and this is associated with a reduction in the levels of AJ components. Furthermore, this correlates with a transient release of tissue tension. Towards the end of the extrusion process, neighboring cells are brought together by the formation and contraction of a supra-cellular actomyosin cables within the neighboring cells. This further restores tissue tension. We conclude that adhesion remodeling and changes in tissue tension are mechanically coordinated, and this represents a mechanism of apoptotic cell extrusion. Furthermore, we reveal that the extrusion process of death-committed LECs is able to mechanically drive histoblast expansion.

Results

Apoptotic cell extrusion coincides with neighboring cell deformation

To explore the effects of extrusion of apoptotic LECs on histoblast expansion, we

Development • Advance article

collected confocal images of the surface of wild-type pupae expressing a *D*E-cad::GFP (*Drosophila* E-cadherin GFP). We found that boundary LECs undergo apical constriction (filled circle in Fig. 1b, Movie 2) and basal extrusion (Movie 3). Concurrently, histoblast cells surrounding apoptotic LECs exhibited biased cell shape deformations (Fig. 1b). Histoblasts that directly contact apoptotic LECs become progressively elongated (yellow dotted line in Fig. 1b). The next-to-nearest-neighbor histoblasts also elongated (white and magenta dotted lines in Fig. 1b). With time, the space originally occupied by the apoptotic LECs was covered by neighboring cells. To quantify histoblast deformation upon boundary LEC extrusion, we monitored cell elongation by measuring the anisotropy of cell shape (Materials and Methods, Fig. 1c, Movie 4). Analyzing the anisotropy revealed that histoblast elongation correlated with LEC extrusion (Fig. 1c), and the degree of elongation decayed as a function of the distance from the extruding cell (Fig. S1a). These observations indicated that the mechanical impact of apoptotic cell extrusion was not restricted to the nearest-neighbor histoblast, but propagated to the next-to-nearest-neighbor cells. The elongated histoblasts (Fig. 1b) underwent either cell division or cell-cell junction remodeling after cell extrusion had completed, and did not maintain their elongated shape (Fig. S2). These rearrangements, however, had no impact on tissue expansion, with the edge of the histoblasts remaining in place after cell extrusion was complete (Fig. S2). This suggests that the mechanical impact of boundary LEC apoptosis on tissue expansion is preserved even after the completion of LEC extrusion.

To further examine the kinematics of extruding LECs, we analyzed the

Development • Advance article

temporal progression of cell shape changes. Boundary LECs exhibited an apical constriction in the course of cell extrusion (Fig. 1d). The time in which the cell area transitioned, $\tau_{area,}$ was defined as the time when the cell started to constrict with higher speed (Materials and Methods, Fig. S3). Intriguingly, the boundary LECs exhibited a characteristic kinematics before and after τ_{area}. The deformation in the shape of an extruding LEC was local and anisotropic before τ_{area}. Here, the major deformation was at the cell boundary adjacent to the growing histoblasts (arrow in Fig. 1e), whereas the cell boundaries next to adjacent LECs showed little or no deformation (arrowheads in Fig. 1e). We speculate that the local deformation, before τ_{area}, was due to compressive stress exerted by proliferating histoblasts, which caused LECs to be passively deformed. By contrast, the contraction of the dying LEC was more isotropic after τ_{area} (Fig. 1e'), which may have been due to the contraction of actomyosin rings formed upon apoptosis. The different kinematics of apoptotic LECs before and after τ_{area} were further supported by quantitative measurements of the cell shape (Fig. S4). Moreover, quantification of a non-extruding LEC that was next to an LEC undergoing extrusion, revealed that although it was static before $\tau_{area,}$ it exhibited local deformations in response to the extrusion of its neighboring cell (Fig. S5a). In this case, the major deformation after τ_{area} was at the cell boundary adjacent to extruding LEC. The cell boundaries away from the cell undergoing extrusion showed little or no deformation (Fig. S5b-b'). Together, we found that the effect of boundary LEC extrusion was restricted to the nearest-neighbor LECs, but propagated into several layers of histoblasts.

Development • Advance article

We further noticed that apoptosis of non-boundary LECs was not strongly associated with histoblast deformation (Fig. S6). Hereafter we focus on the apoptotic process of boundary LECs, which mechanically contributes to histoblast expansion.

Caspase-3 activation precedes apical constriction in apoptotic cells

To clarify the time at which apical constriction commenced, with respect to apoptotic signaling, we monitored caspase activity in LECs by imaging pupae incorporating a genetically encoded fluorescence resonance energy transfer (FRET) based caspase-3-like DEVDase (hereafter referred to as caspase-3) sensor (SCAT3) (Takemoto et al., 2003, Nakajima et al., 2011, Levayer et al., 2016). This sensor displayed a reduced FRET ratio as caspase-3 activation increased (Fig. 2a, Materials and Methods). We used the bipartite GAL4-UAS system (Brand and Perrimon, 1993) to express SCAT3 in the pupal epithelium, including LECs, by *tsh*-GAL4. To monitor the apical constriction of apoptotic LECs in parallel with caspase-3 activity, we imaged *D*E-cad::Tomato^{KI} (Huang et al., 2009) together with SCAT3 (Fig. 2b). Caspase-3 activity progressively increased with time (Fig. 2a, Movie 5, orange line in Fig. 2c). We quantified when caspase-3 activation was initiated as τ_{Cas3}, the time when the cell started to show higher caspase-3 activity (Fig. S3). The time delay between τ_{area} and τ_{Cas3} indicated that the initiation of caspase-3 activation preceded the onset of apical constriction (Fig. 2d). Qualitatively, our data are in an agreement with recent findings from apoptotic extrusion in *Drosophila* notum (Levayer et al., 2016).

Development • Advance article

Remodeling of AJs during apoptotic cell extrusion

To understand how AJs and the associated cytoskeleton were remodeled in the course of LEC apoptosis, we examined the distribution of E-cad (*ubi-D*E-cad::GFP) and Myosin II [non-muscle Myosin II regulatory light chain (Spaghetti-squash - Sqh), MyoII::mCherry]. Stills from time-lapse movies showed that the level of E-cad at the interfaces between apoptotic LECs and neighboring cells, including both histoblasts and non-apoptotic LECs, was reduced (arrowheads in Fig. 3a-a', Movie 6). By contrast, there was no change in the level of *D*E-cad::GFP at cell junctions of neighboring cells, away from the interface (double-arrows in Fig. 3a'). Concomitant to the reduction of E-Cad, MyoII distribution around the periphery of apoptotic LECs showed two myosin cable-like structures (arrows and double-arrows in Fig. 3b). Merged images of E-cad and MyoII (Fig. 3c) indicated that the supra-cellular cable was in the neighboring cells (double-arrows in Fig. 3b,d, referred to as 'outer' cable) while the other cable was in the apoptotic cell (arrows in Fig. 3b,d, referred to as 'inner' cable). The distribution of actin resembled that of MyoII (Fig. S7). We further noticed that E-cad accumulated between the two neighboring cells (arrows in Fig. 3c'). These loci could link the actomyosin cables, thereby forming a supra-cellular actomyosin purse-string-like structure. Importantly, upon completion of apical constriction, *de novo* AJs were formed between the non-apoptotic neighboring cells (t=45min in Fig. 3a, Fig. S8).

To further characterize the progressive reduction of E-cad levels at the interfaces between apoptotic LECs and their neighboring cells, we imaged a GFP knock-in fly line that replaced the endogenous *D*E-cad (*D*E-cad::GFP^{KI}) (Huang et al.,

Development • Advance article

2009). The level of E-cad at the interface between apoptotic LECs and neighboring cells progressively decreased with time (Fig. 3e) and the initiation of the decrease in the level of E-cad τ_{EcadKI} followed the onset of apical constriction τ_{area} (Fig. 3e-f). Furthermore, we found that E-cad levels between pupae with 2 copies of E-cad (E-cad::GFP^{KI}, τ_{EcadKI_red}, 38.3±3.4 min after τ_{area}, n=6, Fig. 3f) and 4 copies of E-cad (*ubi*-E-cad::GFP, τ_{Ecad_red}, 36.4±2.9 min, n=9, Fig. S9a) reduced at similar times, indicating the strong reduction in E-Cad levels during apoptosis is insensitive to the expression level of E-Cad.

The other major components of AJs, α- and β-catenin behaved similarly to E-cad (Fig. S9b-c). Flies expressing a β-cat homolog fusion construct, Armadillo::YFP or a *D*α-catenin::RFP fusion marker, both showed a reduction of these components (Fig. S9b-c, Movie 7-8) at the same time that E-cad reduced ($\tau_{\beta\text{-}cat_red}$ and $\tau_{\alpha\text{-}cat_red}$, Fig. S9a). To test the possibility that the reduction in the levels of E-cad from AJs is associated with the cleavage of β-cat at AJs by caspase-3 (Kessler and Muller, 2009), we used a fly line that replaced the endogenous *D*E-cad with a GFP tagged E-cad-αcat fusion protein (*D*E-cad-αcat::GFP) (Morais-de-S· and Sunkel, 2013). Similar to E-cad, the level of this fusion protein was reduced during extrusion (Fig. S9a,d). This suggests that it is the cleavage of β-cat from a cytoplasmic pool of the protein, rather than the β-cat linking E-cad with αcat in AJs, that plays a role in the reduction of E-cad. Moreover, we cannot rule out the possibility that the reduction in the levels of E-cad is due to the cleavage of the cytoplasmic region of E-cad by caspase-3 (Bannerman et al., 1998).

The observation that two myosin cables form when E-cad is reduced, suggests

Development • Advance article

a loosening of E-cad-dependent cell-cell adhesion. To follow the kinematics of cell-cell contacts during apoptotic cell extrusion, we visualized the overall plasma membrane using the PH domain of PLCγ fused to GFP (PH::GFP) together with MyoII::mCherry. The plasma membranes of apoptotic and neighboring cells sometimes, but not always, detached at the apical section of the cell once the separation of the two myosin cables became apparent (Fig. 3g and S10). In this case, the myosin cables of each cell were approximately at the edge of plasma membranes (Fig. 3g'). By contrast, the two plasma membranes of apoptotic and neighboring cells could maintain their contacts even when the two myosin cables became apparent (Fig. S11).

To gain insight into the dynamics of cell-cell contacts at the basolateral section of the cell, we analyzed the behavior of septate junctions (SJs). These are positioned basal to AJs in *Drosophila* in an opposite orientation relative to that of tight junctions, the functional equivalent of SJs in vertebrates (Oda and Takeichi, 2011). We imaged pupae expressing GFP tagged Neuroglian, a cell surface trans-membrane protein essential for SJ function (Nrg::GFP). In contrast to AJs, SJs were stable throughout the apical constriction (Fig. S12, Movie 9). This suggests that the permeability barrier function is preserved at SJs even when AJs are disengaged during apoptosis of LECs.

Together, our results show that the AJs between dying cells and their neighbors rearranged during apoptosis, and this is associated with a reduction in the levels of AJ components.

Development • Advance article

MyoII accumulates in apoptotic and neighboring cells at different times during apoptosis

To further characterize the formation of actomyosin cables in apoptotic LECs (inner cable), or in neighboring cells (outer cable), we quantified the temporal progression of MyoII accumulation in pupae expressing GFP tagged MyoII (MyoII::GFP), in either histoblasts by *Esg*-GAL4, or LECs by *Eip71CD*-GAL4 (Fig. 4). These flies also ubiquitously expressed MyoII::mCherry. In GFP positive histoblasts, which were considered non-dying neighboring cells, MyoII::GFP was found to accumulate within the vicinity of the apoptotic boundary LECs (double-arrows in Fig. 4a, Movie 10). This accumulation commenced when the space between the two MyoII cables became apparent (t=60, arrowhead and arrow in Fig. 4a) and increased with time (Fig. 4b). The time when MyoII started to accumulate τ_{outer_MyoII} was 35.7±3.8 min after τ_{area} (n=9, Fig. 4e, Materials and Methods), with non-significant differences to the timing of E-cad reduction. This indicated that the initiation of MyoII accumulation in neighboring cells coincided with remodeling of AJs. Moreover, the intensity of MyoII in neighboring LECs increased concurrently with MyoII in histoblasts (t=60 and 70, arrowheads in Fig. 4a), suggesting the formation of the actomyosin cables in the two different cell types (i.e., non-dying histoblasts and LECs) was coordinated. To facilitate the analysis of MyoII accumulation in apoptotic LECs, we quantified the intensity of the MyoII::GFP signal (Fig. 4c, Movie 11) that originated solely from the cell periphery of apoptotic LECs facing histoblasts (arrows in Fig. 4c'). In dying cells, MyoII started increasing as apical constriction commenced (τ_{inner_MyoII}, Fig. 4d-e). This observation implied that the actomyosin cable in the apoptotic cell is present before the reduction

Development • Advance article

of E-cad levels.

Altogether, the analyses of MyoII distribution showed that the formation of actomyosin cables in apoptotic and neighboring cells occur at different times, implying that the two cables contribute at different stages of apoptotic cell extrusion.

Actomyosin cable formation, apical constriction, and a reduction in E-cad levels upon apoptosis are caspase-3 dependent

In apoptotic LECs, caspase-3 is activated prior to the initiation of apical constriction (Fig. 2), the reduction in E-cad levels (Fig. 3), and the accumulation of MyoII in dying and neighboring cells (Fig. 4). To investigate the role of caspase-3 in apoptotic cell extrusion, we ectopically expressed a baculovirus caspase inhibitor, p35, in the majority of LECs by *Eip71CD*-GAL4. This fly also ubiquitously expressed *D*E-cad::GFP^{KI} or MyoII::GFP. As previously reported (Ninov et al., 2007), tissue expansion (Fig. S13a) and the extrusion of LECs, are delayed when p35 is expressed, with cells requiring more time to leave the tissue (Fig. 5a, Movie 12. Pink line in Fig. 5b). The number of LEC's undergoing extrusion was reduced by more than 90%, however extrusion did not cease completely (38.7±3.3 and 3.0±1.0 cells within 5 hours in wild-type and p35 pupae, respectively). During extrusion of p35-positive LECs, no significant reduction in E-cad levels (Fig. 5a. Blue line in Fig. 5b) was observed. Similarly, MyoII did not accumulate in either the extruding or neighboring cells (Fig. 5c-d, S13b, Movie 13), and the space between MyoII cables (Fig. 5c) was not observed. These results indicated that the extrusion of p35 expressing LECs is different in nature

Development • Advance article

to that of caspase positive wild-type LECs. Indeed, Ninov et al reported that extruded p35-positive cells were viable under the epithelium, and were not engulfed by haemocytes (Ninov et al., 2007). We speculate that the extrusion of p35-positive LECs occurs when they are pushed out by expanding histoblasts (Fig. 1e). Together, our data showed that the formation of actomyosin cables, the apical constriction, and the reduction in E-cad levels observed during wild-type LEC apoptosis are caspase-dependent.

Disruption of MyoII compromises apoptotic cell extrusion, without preventing reduction of E-cad level

To further investigate the mechanism behind the strong reduction in E-cad levels, and to define the contribution of actomyosin contractility in this mechanism, we ectopically expressed *sqh*-RNAi (MyoII regulatory light chain RNAi) in the majority of LECs by *Eip71CD*-GAL4. This fly also ubiquitously expressed either *D*E-cad::GFP^{KI} or MyoII::GFP (Fig. 6). The level of MyoII::GFP (Fig. 6a-b) and phosphorylated myosin regulatory light chain (Fig. S14) in LECs was reduced in *sqh*-RNAi expressing pupae compared to wild-type pupae. This was accompanied by a strongly delayed apical constriction (Fig. 6c-d), a low level of E-cad in the LECs (Fig. S15), and less, if not absent, mechanical impact on the surrounding histoblasts (Fig. S1b), compared to wild-type pupae. We observed a strong reduction of E-cad in all *sqh*-RNAi positive apoptotic cells (arrowheads in Fig. 6e, n=9, Movie 14). Furthermore, we noticed a space existed between MyoII cables (Fig. 6f, n=10 out of 19 cells) in around half of the

Development • Advance article

apoptotic cells. This was in contrast to other cells, where the space was not observed (Fig. 6g, n=9 out of 19 cells). Together, these results suggest that the strong reduction of E-cad in apoptotic LECs could be independent of actomyosin cable contraction, whereas the formation of the space between actomyosin cables, which was normally observed during wild-type LEC apoptosis, required actomyosin contractility.

Disruption of MyoII in neighboring cells strongly delays apoptotic cell extrusion

To understand the role of the supra-cellular actomyosin cable in apoptotic cell extrusion, we sought to impair actomyosin contractility only in neighboring non-dying cells. To this end, we expressed *sqh*-RNAi in a subset of LECs using the mosaic analysis with a repressible cell marker (MARCM) system (Lee and Luo, 1999) (Fig. 7a-b, Movie 15). We then examined apoptosis of wild-type LECs, which were positioned next to RNAi positive LECs (highlighted with blue dotted line in Fig. 7b). In this case, all but one of the neighboring cells were wild-type, and the contractility of the supra-cellular actomyosin cable was therefore only partially affected. First, we qualitatively compared the apical constriction of apoptotic wild-type LECs that were next to RNAi positive cells (hereafter referred to as $LEC_{WT/RNAi}$, highlighted with red dotted line in Fig. 7b) to that of wild-type LECs fully surrounded by wild-type cells (hereafter referred to as $LEC_{WT/WT}$, highlighted with white dotted line in Fig. 7b). This comparison was done on cells in the same pupa. We found that LECs with MyoII-defective neighbors ($LEC_{WT/RNAi}$) exhibited a slower apical constriction, which, compared to controls, also required a longer time to complete (Fig. 7c). Quantitative

Development • Advance article

analyses further supported these observations (Fig. 7d) and we reasoned that this delay was the result of the partially compromised supra-cellular actomyosin cable in neighboring cells. The contour plot of apoptotic $LEC_{WT/RNAi}$ shown in Figure 7b shows that the apical constriction appears to be biased toward the RNAi positive cell (arrow in Fig. 7e). This observation was further supported by tracking the trajectory of the centroid of the apoptotic cell shape (Fig. 7f-f'). These observations suggested that the supra-cellular actomyosin cables with partially defective myosin contraction lead to eccentric deformation of apoptotic cells. Together our data showed that the actomyosin cable that formed in neighboring cells upon apoptosis played an important role in the extrusion process.

Development • Advance article

Tissue tension is transiently released upon E-cad reduction and re-shaped afterwards

The appearance of two actomyosin cables associated with a reduction in E-cad level implied that tissue tension is altered during the apoptotic cell extrusion. Indeed, we found that a subset of neighboring histoblast cell boundaries, which are orthogonal to the interface between apoptotic and neighboring cells, lose their straightness (arrows in Fig. 8a-b), suggesting a release of junctional tension. We further noticed that the cell boundary became straight again when the outer cable contracts (double-arrow in Fig. 8c). Quantification of the linearity of the cell boundaries (Materials and Methods) further supported these observations (Fig. 8d). To characterize the change in tension of neighboring cells during apoptosis, we probed the junctional tension at different stages of apoptosis by laser nano-ablation (Hara et al., 2016) (Fig. 8a'-c', Movie 16). Compared to the control boundaries, the initial recoil velocity after ablation (Materials and Methods), which is the first good approximation of the junctional tension right before ablation, decreased immediately after E-cad levels reduced. (Fig. 8e). Moreover, the recoil velocity increased to an even higher level at the later stages of apoptosis, compared to that of the control boundaries (Fig. 8e). The cell boundaries of neighboring LECs showed the same trend (Fig. S16). Altogether, our results show that tissue tension is transiently released upon the reduction of E-Cad and is re-shaped during the late stages of cell extrusion.

Development • Advance article

Discussion

Progressive remodeling of AJs and redistribution of tensile force upon apoptosis

We report here, the temporal sequence of events during apoptotic cell extrusion, with a focus on the remodeling of AJs, the cytoskeleton, and mechanical tension. After caspase-3 starts to be activated in LECs, those undergoing apoptosis initiate apical constriction (Fig. 2). We reasoned that the initiation of this constriction could be due to a combination of actomyosin cable formation in the dying cell (Fig. 4) and the activity of caspase-3, which assists in the upregulation of actomyosin contractility. Indeed, it has been shown in tissue culture that the cleavage of Rho associated kinase by caspase-3 is involved in phosphorylation and activation of myosin light chain, which regulates actomyosin contractility (Leung et al., 1996). We propose that the actomyosin cable that forms in apoptotic LECs is responsible for the early stages of apoptotic cell extrusion. During apical constriction, the level of AJ components including E-cad strongly reduced in a caspase-3-dependent manner (Fig. 5). In the neighboring non-dying cells, this reduction is found only at the interface between the apoptotic cell and its neighbors (Fig. 3a'). Since caspase-3 is not activated in the neighboring cells, we speculate that the reduction of E-cad is a consequence of a loss of trans-interactions between E-cad of the neighboring cell, and E-cad of the apoptotic cell, which undergoes caspase-3-dependent cleavage. This often, but not always, leads to plasma membrane separation (Fig. 3g), which is suggestive of a loosening of AJ-dependent adhesion. Reyes et al reported that anillin organizes and stabilizes actomyosin contractile rings at AJs and its knock-down is associated with a reduction of E-cad and β-cat levels at AJs, leading to AJ disengagement (Reyes et al., 2014). A gradual decrease in the level of E-cad (Fig. 3e), and a gradual increase in MyoII accumulation

Development • Advance article

in apoptotic cells (Fig. 5d) was observed prior to the strong reduction of E-cad levels. This leads us to hypothesize that mechanical tension exerted on the cell interface between apoptotic LECs and neighboring cells by the contraction of the actomyosin cable, which forms in the apoptotic cell, is large enough to rupture the weakened contacts between plasma membranes at AJs upon the strong reduction of E-cad levels. Interestingly, and by contrast, there are cases when AJs are not disengaged even after the level of E-cad is reduced. In these cases the cells exhibit a separation of actomyosin cables from the membrane (Fig. S11). We speculate that the state of cell-cell contacts at AJs, i.e., whether they will disengage or remain engaged during apoptosis, is dependent on which of the following links is weaker: The link between two plasma membranes, or the link between the plasma membrane and the actomyosin cable. Both of these links would be weakened by a strong, albeit incomplete, reduction of E-cad levels. When the former is weaker than the latter, the two plasma membranes could be detached. When the former is stronger than the latter, the two plasma membranes could remain in contact, and the actomyosin cable could be detached from the plasma membrane.

In parallel with the reduction of E-cad levels and the associated release of tension (Fig. 8), a supra-cellular actomyosin cable begins to form in neighboring cells (Fig. 4). These observations prompt us to speculate that the release of tissue tension triggers MyoII accumulation in neighboring cells. Subsequent contraction of this outer ring helps to reshape tissue tension, which is transiently released when E-cad is reduced. As a consequence, the neighboring cells are stretched (Fig. 1). Upon

Development • Advance article

completion of apical constriction, neighboring non-apoptotic cells form *de novo* AJs (Fig. S8) and the stretched cells undergo cell division and/or cell-cell contact rearrangement (Fig. S2). These processes allow a relaxation of the high tension associated with the stretching of cells (Fig. 7e). Finally, our measurements of caspase-3 activity (Fig. 2), and our observations from caspase inhibition experiments (Fig. 5), help us to conclude that the characteristics associated with apoptotic cell extrusion reported in this study are the consequences of the apoptotic process, rather than the cause.

Apoptosis mechanically drives tissue expansion

In addition to the progressive remodeling of AJs and modulation of tissue tension during apoptosis, we examined the mechanical role of apoptosis 'apoptotic force' in tissue morphogenesis, which has been proposed, demonstrated, and discussed (Stenn et al., 1998, Toyama et al., 2008, Suzanne et al., 2010, Teng and Toyama, 2011, Miura, 2012, Kuranaga, 2012, Monier et al., 2015, Okuda et al., 2015, Pérez-Garijo and Steller, 2015, Monier and Suzanne, 2015). We show that the mechanical force generated by the contraction of actomyosin cables formed when LECs undergo apoptosis, especially boundary LECs, promotes tissue expansion (Fig. 1, S1), along with histoblast proliferation and migration (Ninov et al., 2007, Ninov et al., 2010). Nonetheless, we can't rule out the possibility that this apical contraction is in part driven by a decrease in cell volume, which can be triggered by caspase activation (Saias et al., 2015). Intriguingly, we found that apoptosis of non-boundary LECs did not affect tissue

Development • Advance article

expansion (Fig. S5-6). This raised the possibility that the mechanical influence of apoptosis in neighboring tissues is dependent not only on the physical connections between cells, but also on the mechanical properties of cells, including cell compliance. If a tissue is soft, for instance, the tensile forces generated by apoptotic process could be absorbed by nearest-neighbor cells and would not propagate to cells further than a single cell away. We speculate that the apoptotic process could mechanically contribute to cell death-related morphogenesis, only when apoptosis takes place at optimal mechanical properties of a tissue.

Here, we present a framework for understanding how cell adhesions and tissue tension are progressively modulated during apoptosis in a developing epithelium (Fig. S17). We conclude that tissue tension reshaping, including the transient release of tension upon a reduction in the levels of AJ components, represents a mechanism of apoptotic cell extrusion. It would be important to explore how this transient modulation in mechanical tension would further influence the biochemical nature of neighboring non-apoptotic cells.

Development • Advance article

Materials and Methods

Fly husbandry, Sample preparation and Live Imaging

Flies and crosses were raised on standard media at 25degree. Staged pupae were collected, dissected, mounted and imaged as previously described (Ninov and Martin-Blanco, 2007). Refer to Supplemental Materials and Methods for a complete list of fly strains and, details of microscopy used.

Image analyses and quantification

All confocal images shown (except Fig. 8, S12, and S16) are maximum projection of ~3µm along the apical-basal axis of a cell around AJs. Images shown in Fig, 8, S12, and S16 are single confocal sections at AJs. We used ImageJ, Packing Analyzer V2.0 (Aigouy et al., 2010), and/or Matlab software (MathWorks, MA, USA) for image quantification and subsequent analyses. The details can be found in Supplemental Materials and Methods.

Acknowledgements

We acknowledge the following for the generous gift of flies: M.Affolter, H.Hong, D.P.Kiehart, E.Kuranaga, T.Lecuit, A.C.Martin, M.Miura, K.Sugimura, Bloomington Stock Center, Kyoto Drosophila Genetic Resource Center, and Vienna Drosophila RNAi Center. We thank Microscopy Core of MBI, Bioimaging and Biocomputing Facility of TLL, and Microscopy Rennes Imaging Center. We also thank E.Kuranaga, B.Ladoux, E.Martın-Blanco, M.Sheetz, M.Sudol, K.Sugimura, and MBI Science

Development • Advance article

Communication Core (S.Wolf) for helpful discussions and critical reading of the manuscript.

Competing interests

The authors declare no competing or financial interests.

Author contributions

X.T. and Y.T. designed the research and prepared the manuscript. X.T., R.L.B., and Y.T. edit the manuscript. X.T., R.L.B., and Y.T. performed the experiments and analyses. L.Q. contributed new reagents. Y.T. oversaw the project.

Funding

This work was supported by an NUS Research Scholarship (to X.T.), Mechanobiology Institute and National University of Singapore Startup Grants (to Y.T.), Temasek Life Sciences Laboratory (to Y.T.), and a Singapore Ministry of Education Tier 2 grant (MOE2015-T2-1-116 to Y.T.). R.L.B. and Y.T. thank the support by the PHC Merlion Programme n° 5.14.13 of the Institut Français de Singapour, under administrative supervision of the French Ministry of Foreign Affairs, and the National University of Singapore.

Supplemental information

Supplemental Information, includes Supplemental Materials and Methods, sixteen figures, and sixteen movies, available online

Development • Advance article

References

Aigouy, B., Farhadifar, R., Staple, D.B., Sagner, A., Roper, J.C., Julicher, F. & Eaton, S. (2010). Cell flow reorients the axis of planar polarity in the wing epithelium of Drosophila. *Cell,* 142**,** 773-86.

Bannerman, D.D., Sathyamoorthy, M. & Goldblum, S.E. (1998). Bacterial Lipopolysaccharide Disrupts Endothelial Monolayer Integrity and Survival Signaling Events through Caspase Cleavage of Adherens Junction Proteins. *Journal of Biological Chemistry,* 273**,** 35371-35380.

Bischoff, M. & Cseresnyes, Z. (2009). Cell rearrangements, cell divisions and cell death in a migrating epithelial sheet in the abdomen of Drosophila. *Development,* 136**,** 2403-2411.

Brancolini, C., Lazarevic, D., Rodriguez, J. & Schneider, C. (1997). Dismantling Cell–Cell Contacts during Apoptosis Is Coupled to a Caspase-dependent Proteolytic Cleavage of β-Catenin. *The Journal of Cell Biology,* 139**,** 759-771.

Brand, A.H. & Perrimon, N. (1993). Targeted gene expression as a means of altering cell fates and generating dominant phenotypes. *Development,* 118**,** 401-15.

Eisenhoffer, G.T., Loftus, P.D., Yoshigi, M., Otsuna, H., Chien, C.B., Morcos, P.A. & Rosenblatt, J. (2012). Crowding induces live cell extrusion to maintain homeostatic cell numbers in epithelia. *Nature,* 484**,** 546-U183.

Hara, Y., Shagirov, M. & Toyama, Y. (2016). Cell Boundary Elongation by Non-autonomous Contractility in Cell Oscillation. *Current biology : CB,* 26**,** 2388-96.

Harris, T.J. & Tepass, U. (2010). Adherens junctions: from molecules to morphogenesis. *Nat Rev Mol Cell Biol,* 11**,** 502-14.

Huang, J., Zhou, W., Dong, W., Watson, A.M. & Hong, Y. (2009). Directed, efficient, and versatile modifications of the Drosophila genome by genomic engineering. *Proceedings of the National Academy of Sciences,* 106**,** 8284-8289.

Jacobson, M.D., Weil, M. & Raff, M.C. (1997). Programmed cell death in animal development. *Cell,* 88**,** 347-54.

Kessler, T. & Muller, H.A. (2009). Cleavage of Armadillo/beta-catenin by the caspase DrICE in Drosophila apoptotic epithelial cells. *BMC developmental biology,* 9**,** 15.

Development • Advance article

Kiehart, D.P., Galbraith, C.G., Edwards, K.A., Rickoll, W.L. & Montague, R.A. (2000). Multiple forces contribute to cell sheet morphogenesis for dorsal closure in Drosophila. *Journal of Cell Biology,* 149**,** 471-490.

Kuipers, D., Mehonic, A., Kajita, M., Peter, L., Fujita, Y., Duke, T., Charras, G. & Gale, J.E. (2014). Epithelial repair is a two-stage process driven first by dying cells and then by their neighbours. *Journal of cell science,* 127**,** 1229-41.

Kuranaga, E. (2012). Beyond apoptosis: caspase regulatory mechanisms and functions in vivo. *Genes Cells,* 17**,** 83-97.

Kuranaga, E., Matsunuma, T., Kanuka, H., Takemoto, K., Koto, A., Kimura, K. & Miura, M. (2011). Apoptosis controls the speed of looping morphogenesis in Drosophila male terminalia. *Development,* 138**,** 1493-1499.

Lecuit, T. & Yap, A.S. (2015). E-cadherin junctions as active mechanical integrators in tissue dynamics. *Nat Cell Biol,* 17**,** 533-9.

Lee, T. & Luo, L. (1999). Mosaic analysis with a repressible cell marker for studies of gene function in neuronal morphogenesis. *Neuron,* 22**,** 451-61.

Leung, T., Chen, X.Q., Manser, E. & Lim, L. (1996). The p160 RhoA-binding kinase ROK alpha is a member of a kinase family and is involved in the reorganization of the cytoskeleton. *Molecular and cellular biology,* 16**,** 5313-27.

Levayer, R., Dupont, C. & Moreno, E. (2016). Tissue Crowding Induces Caspase-Dependent Competition for Space. *Current Biology,* 26**,** 670-677.

Lubkov, V. & Bar-Sagi, D. (2014). E-cadherin-mediated cell coupling is required for apoptotic cell extrusion. *Current Biology,* 24**,** 868-874.

Manjon, C., Sanchez-Herrero, E. & Suzanne, M. (2007). Sharp boundaries of Dpp signalling trigger local cell death required for Drosophila leg morphogenesis. *Nature Cell Biology,* 9**,** 57-U66.

Marinari, E., Mehonic, A., Curran, S., Gale, J., Duke, T. & Baum, B. (2012). Live-cell delamination counterbalances epithelial growth to limit tissue overcrowding. *Nature,* 484**,** 542-U177.

Meghana, C., Ramdas, N., Hameed, F.M., Rao, M., Shivashankar, G.V. & Narasimha, M. (2011). Integrin adhesion drives the emergent polarization of active cytoskeletal

Development • Advance article

stresses to pattern cell delamination. *Proceedings of the National Academy of Sciences of the United States of America,* 108**,** 9107-12.

Michael, M., Meiring, J.C.M., Acharya, B.R., Matthews, D.R., Verma, S., Han, S.P., Hill, M.M., Parton, R.G., Gomez, G.A. & Yap, A.S. (2016). Coronin 1B Reorganizes the Architecture of F-Actin Networks for Contractility at Steady-State and Apoptotic Adherens Junctions. *Developmental Cell,* 37**,** 58-71.

Miura, M. (2012). Apoptotic and nonapoptotic caspase functions in animal development. *Cold Spring Harbor perspectives in biology,* 4.

Monier, B., Gettings, M., Gay, G., Mangeat, T., Schott, S., Guarner, A. & Suzanne, M. (2015). Apico-basal forces exerted by apoptotic cells drive epithelium folding. *Nature,* 518**,** 245-U252.

Monier, B. & Suzanne, M. (2015). Chapter Twelve-The Morphogenetic Role of Apoptosis. *Current topics in developmental biology,* 114**,** 335-362.

Morais-De-S·, E. & Sunkel, C. (2013). Adherens junctions determine the apical position of the midbody during follicular epithelial cell division. *EMBO reports,* 14**,** 696-703.

Muliyil, S., Krishnakumar, P. & Narasimha, M. (2011). Spatial, temporal and molecular hierarchies in the link between death, delamination and dorsal closure. *Development,* 138**,** 3043-54.

Nakajima, Y.-I., Kuranaga, E., Sugimura, K., Miyawaki, A. & Miura, M. (2011). Nonautonomous Apoptosis Is Triggered by Local Cell Cycle Progression during Epithelial Replacement in Drosophila. *Molecular and Cellular Biology,* 31**,** 2499-2512.

Ninov, N., Chiarelli, D.A. & Martin-Blanco, E. (2007). Extrinsic and intrinsic mechanisms directing epithelial cell sheet replacement during Drosophila metamorphosis. *Development,* 134**,** 367-379.

Ninov, N. & Martin-Blanco, E. (2007). Live imaging of epidermal morphogenesis during the development of the adult abdominal epidermis of Drosophila. *Nature Protocols,* 2**,** 3074-3080.

Ninov, N., Menezes-Cabral, S., Prat-Rojo, C., Manjón, C., Weiss, A., Pyrowolakis, G., Affolter, M. & Martín-Blanco, E. (2010). Dpp Signaling Directs Cell Motility and

Development • Advance article

Invasiveness during Epithelial Morphogenesis. *Current Biology,* 20**,** 513-520.

Oda, H. & Takeichi, M. (2011). Structural and functional diversity of cadherin at the adherens junction. *The Journal of cell biology,* 193**,** 1137-1146.

Okuda, S., Inoue, Y., Eiraku, M., Adachi, T. & Sasai, Y. (2015). Modeling cell apoptosis for simulating three-dimensional multicellular morphogenesis based on a reversible network reconnection framework. *Biomechanics and modeling in mechanobiology***,** 1-12.

Pérez-Garijo, A. & Steller, H. (2015). Spreading the word: non-autonomous effects of apoptosis during development, regeneration and disease. *Development,* 142**,** 3253-3262.

Reyes, C.C., Jin, M., Breznau, E.B., Espino, R., Delgado-Gonzalo, R., Goryachev, A.B. & Miller, A.L. (2014). Anillin regulates cell-cell junction integrity by organizing junctional accumulation of Rho-GTP and actomyosin. *Current Biology,* 24**,** 1263-1270.

Riedl, S.J. & Shi, Y. (2004). Molecular mechanisms of caspase regulation during apoptosis. *Nat Rev Mol Cell Biol,* 5**,** 897-907.

Rosenblatt, J., Raff, M.C. & Cramer, L.P. (2001). An epithelial cell destined for apoptosis signals its neighbors to extrude it by an actin- and myosin-dependent mechanism. *Current Biology,* 11**,** 1847-1857.

Saias, L., Swoger, J., D'angelo, A., Hayes, P., Colombelli, J., Sharpe, J., Salbreux, G. & Solon, J. (2015). Decrease in Cell Volume Generates Contractile Forces Driving Dorsal Closure. *Developmental cell,* 33**,** 611-21.

Shen, J. & Dahmann, C. (2005). Extrusion of cells with inappropriate Dpp signaling from Drosophila wing disc epithelia. *Science,* 307**,** 1789-1790.

Sokolow, A., Toyama, Y., Kiehart, D.P. & Edwards, G.S. (2012). Cell Ingression and Apical Shape Oscillations during Dorsal Closure in Drosophila. *Biophysical Journal,* 102**,** 969-979.

Stenn, K., Parimoo, S. & Prouty, S. (1998). Growth of the hair follicle: a cycling and regenerating biological system. *Molecular basis of epithelial appendage morphogenesis***,** 111-130.

Development • Advance article

Suzanne, M., Petzoldt, A.G., Spéder, P., Coutelis, J.-B., Steller, H. & Noselli, S. (2010). Coupling of apoptosis and L/R patterning controls stepwise organ looping. *Current Biology,* 20**,** 1773-1778.

Takeichi, M. (2014). Dynamic contacts: rearranging adherens junctions to drive epithelial remodelling. *Nat Rev Mol Cell Biol,* 15**,** 397-410.

Takemoto, K., Nagai, T., Miyawaki, A. & Miura, M. (2003). Spatio-temporal activation of caspase revealed by indicator that is insensitive to environmental effects. *The Journal of cell biology,* 160**,** 235-43.

Teng, X. & Toyama, Y. (2011). Apoptotic force: active mechanical function of cell death during morphogenesis. *Development, growth & differentiation,* 53**,** 269-76.

Toyama, Y., Peralta, X.G., Wells, A.R., Kiehart, D.P. & Edwards, G.S. (2008). Apoptotic force and tissue dynamics during Drosophila embryogenesis. *Science,* 321**,** 1683-1686.

Yamaguchi, Y., Shinotsuka, N., Nonomura, K., Takemoto, K., Kuida, K., Yosida, H. & Miura, M. (2011). Live imaging of apoptosis in a novel transgenic mouse highlights its role in neural tube closure. *Journal of Cell Biology,* 195**,** 1047-1060.

Development • Advance article

Figures

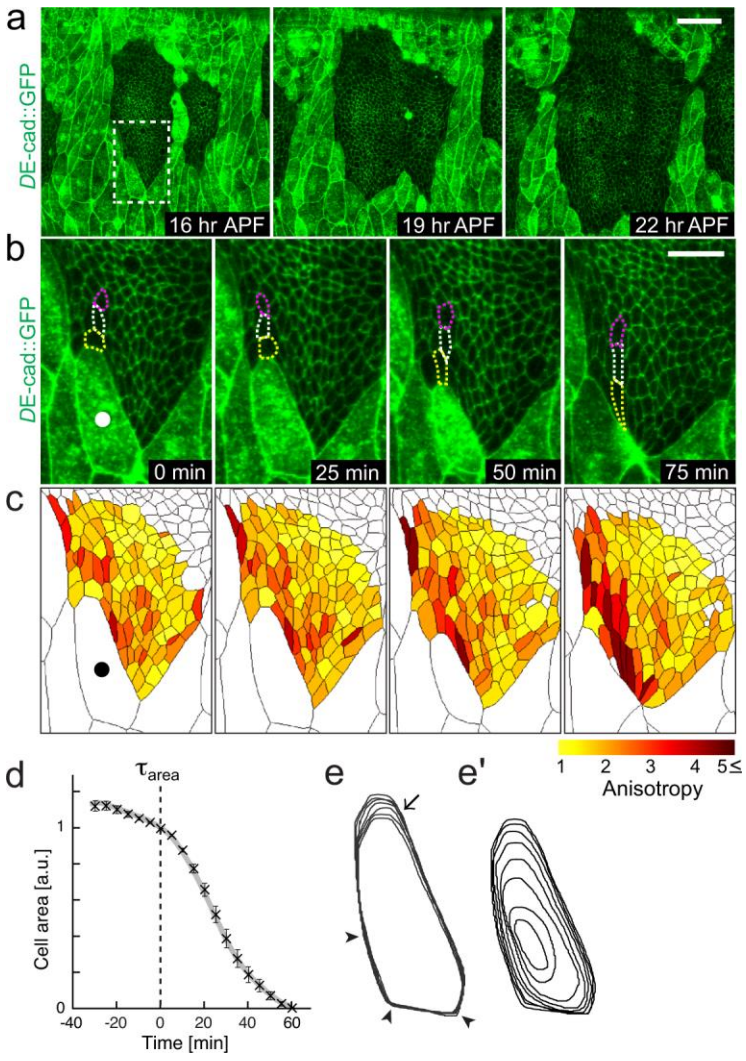


Fig. 1. Kinematics of apoptotic LEC and surrounding histoblast cells during histoblast expansion.

(a) Confocal images of wild-type pupa expressing *D*E-cad::GFP, showing anterior and posterior dorsal histoblast nests and larval epithelial cells (LECs) at 16, 19, and 22hours

Development • Advance article

after puparium formation (APF) (Movie 1). (b) High magnification of the dotted region depicted in (a) (Movie 2). Imaging started at 0 min. An apoptotic LEC (filled circle), the nearest-neighbor cell (yellow dashed line), and the cells that are not directly attached to apoptotic LEC (white and magenta dashed lines) are highlighted. Anterior is to the left and ventral to the top in all figures. (c) Color-enhanced reproduction of the confocal images from (b) (Movie 4). Colors denote the anisotropy of cell shape. The darker colors represent more elongated cells. (d) Graph plotting the normalized apical cell area of apoptotic cells over time (n=21). τ_{area} (gray dotted line) denotes the time when the cell started to constrict with higher speed. Error bars indicate SEM. (e) Contour plots showing the deformation in the shape of the apoptotic cell highlighted in (b) prior to τ_{area}. Cell deformation is local, as highlighted by the arrow. Arrowheads highlight the cell boundary with little deformation. (e') Contour plots of the apoptotic cell from τ_{area} onwards. Scale bars, 50μm (a) and 20μm (b).

Development • Advance article

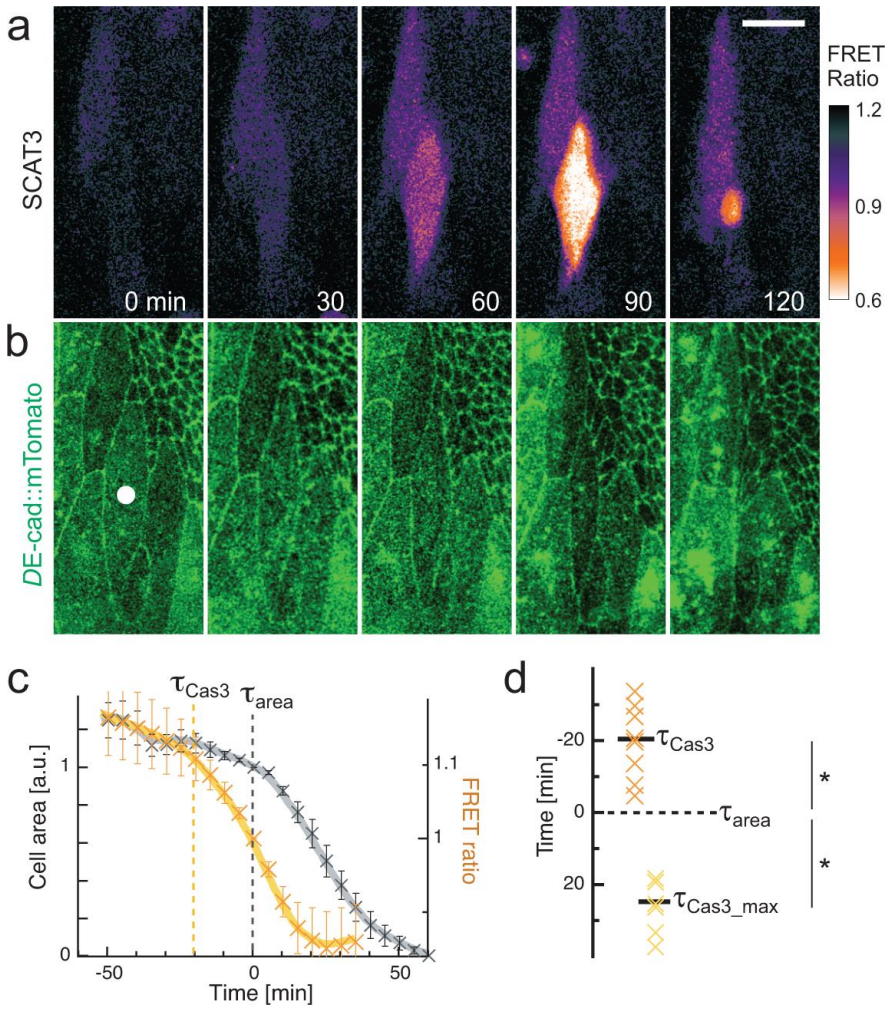


Fig. 2. Caspase activation precedes apical constriction in apoptotic LECs.

(a, b) Confocal images of wild-type pupa expressing FRET-based caspase-3 sensor SCAT3 and *D*E-cad::mTomato (Movie 5). Imaging started at 0min. (a) Stills from a time-lapse movie showing caspase activity in LECs. The pseudo-color represents the fluorescent intensity ratio (Venus/ECFP). (b) Stills from a time-lapse movie of E-cad. An apoptotic LEC highlighted with a filled circle. (c) Graphs plotting the normalized cell apical area (gray) and caspase-3 activity (orange) of the apoptotic cell over time (n=8). Gray and orange dotted lines represent τ_{area} and the time when the cell started to show higher FRET ratio τ_{Cas3}, respectively. Error bars indicate SEM. (d) Time delays between τ_{area} and either τ_{Cas3} or the time caspase reaches its maximum value τ_{Cas3_max} (n=8, *: P<0.05). Average values are shown as thick horizontal lines. Scale bar, 20μm.

Development • Advance article

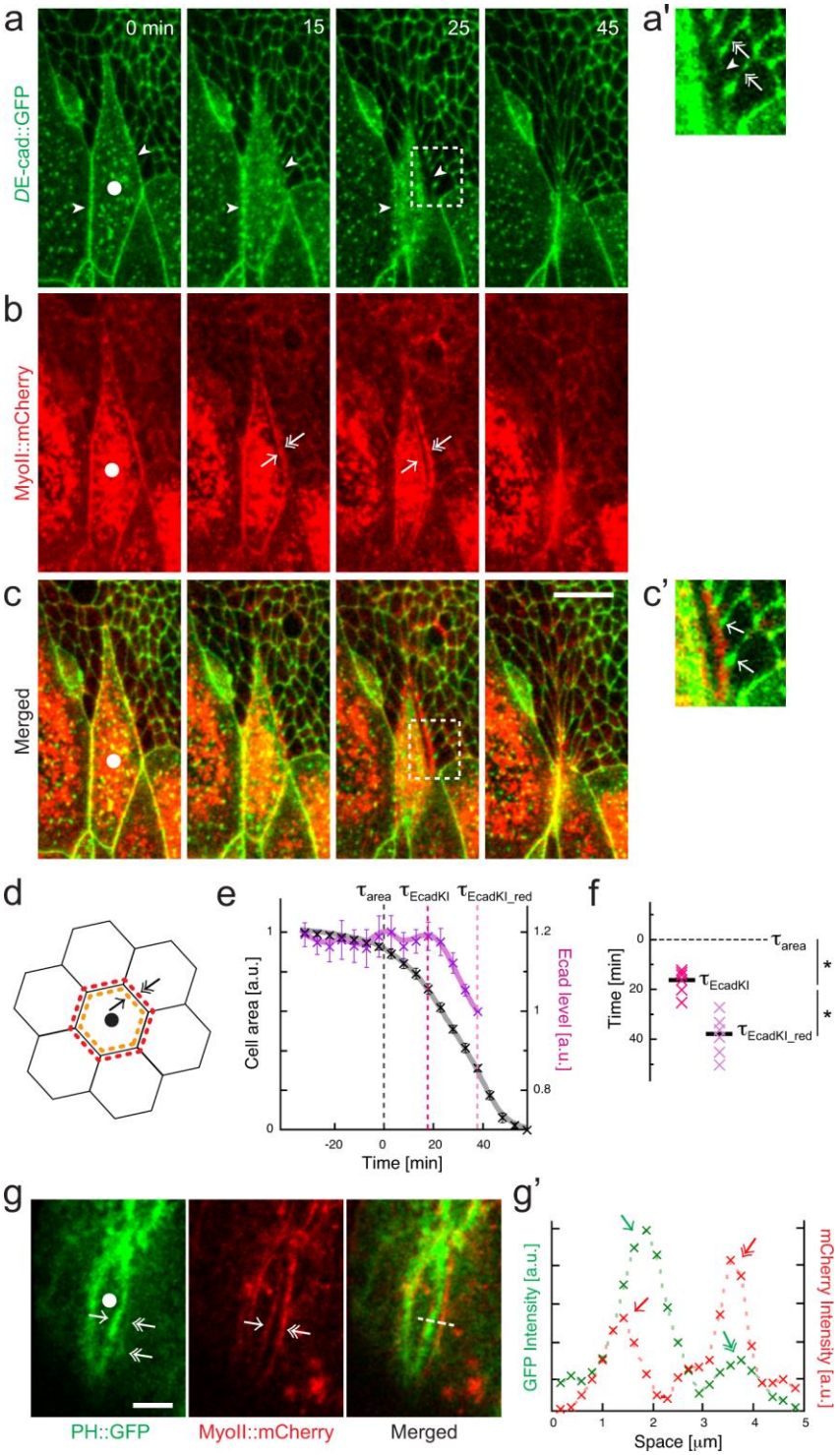


Fig. 3. Reduction of E-Cad levels and AJ remodeling during apical constriction of apoptotic LECs.

(a-c) Confocal images of wild-type pupa expressing *D*E-cad::GFP and MyoII::mCherry

Development • Advance article

(Movie 6). (a) The progression of E-cad reduction at the interface between the apoptotic LEC and neighboring cells (arrowheads). (a') High magnification of the dotted region depicted in (a). E-cad at cell junctions away from the interface (double-arrows) were not reduced. (b) MyoII distribution around the periphery of apoptotic LEC shows two myosin cable-like structures (arrows and double-arrows). (c) Merged images of (a) and (b). (c') High magnification of the dotted region depicted in (c). Arrows show the high accumulation of E-cad at the boundaries between neighboring cells. (d) Schematic (not to scale) showing the actomyosin cable in an apoptotic cell (inner cable, orange dashed-line, arrow) and the supra-cellular actomyosin cable in neighboring cells (outer cable, red dashed-line, double-arrow). (e) Graphs plotting the normalized apical area (gray) and E-cad level (purple) of apoptotic cells of wild-type pupa expressing *D*E-cad::GFP^{KI}, over time (n=6). Error bars indicate SEM. Gray, purple, and pink dotted line denote τ_{area}, the time E-cad starts to decrease τ_{EcadKI}, and the timing of the strong reduction of E-cad levels τ_{EcadKI_red}, respectively. (f) Time delays between τ_{area} and either τ_{EcadKI} or τ_{EcadKI_red} (n=6, *: $P<0.05$). Average values are shown as thick horizontal lines. (g) Confocal images of wild-type pupae expressing the plasma membrane markers PH::GFP and MyoII::mCherry, highlighting the locations of the plasma membrane and myosin cable of the apoptotic cell (arrow) and of the neighboring cells (double-arrows). (g') Line profile of the fluorescence intensity of PH::GFP (green) and MyoII::mCherry (red). The two peaks represent the fluorescence in the apoptotic cell (arrows) and neighboring cell (double-arrows). Scale bars, 20μm (c and g). Apoptotic LECs are highlighted with filled circles.

Development • Advance article

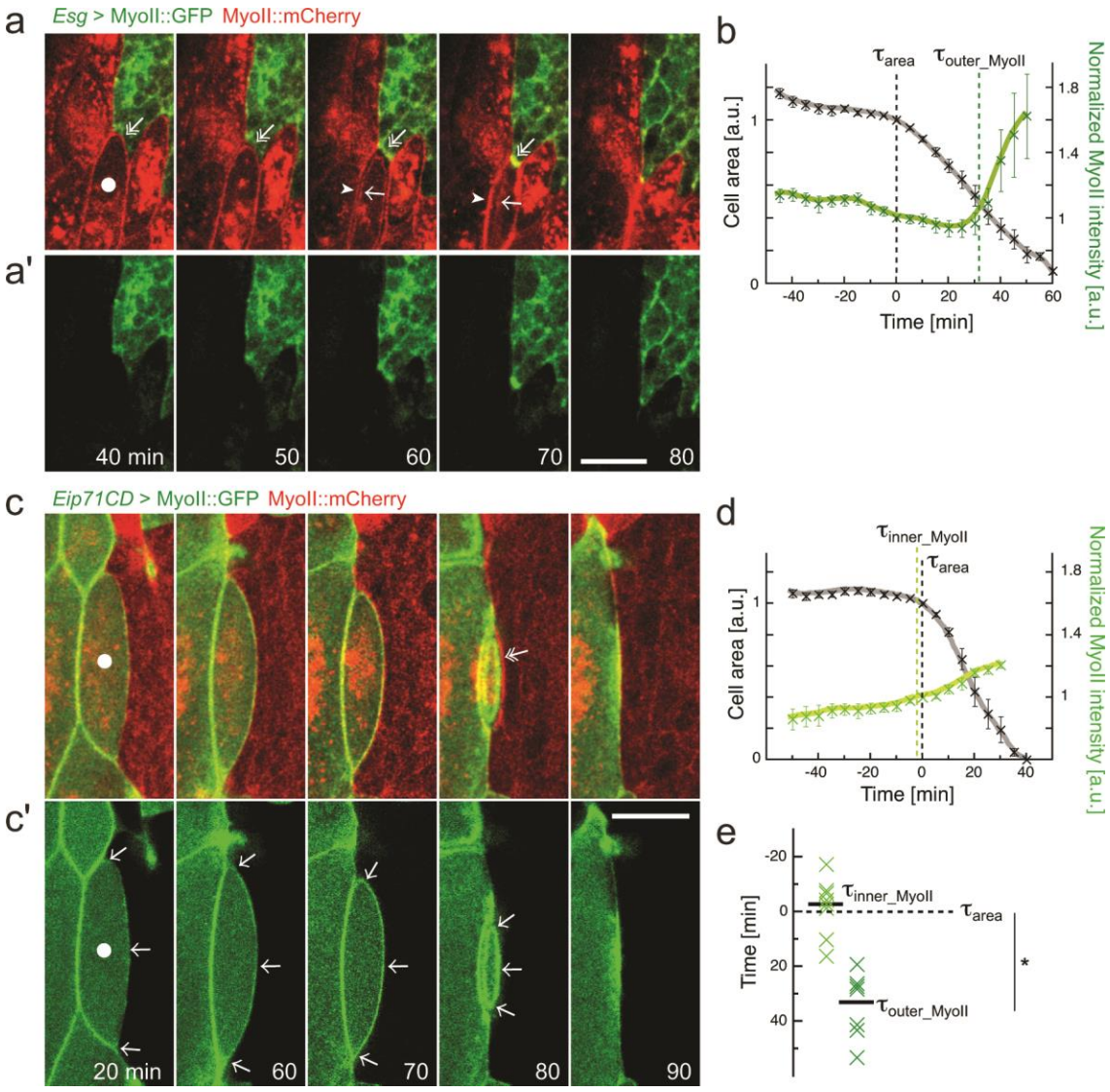


Fig. 4. MyoII accumulates at different times in apoptotic and neighboring cells.

(a-a') Confocal images of wild-type pupa expressing MyoII::GFP only in histoblast, and MyoII::mCherry ubiquitously (Movie 10). (a) Arrows and arrowheads show MyoII accumulation in the apoptotic LEC and in the neighboring LECs, respectively. (a') MyoII::GFP images. (b) Graphs showing the normalized cell area of dying LECs (gray) and MyoII intensity of neighboring histoblast cells (dark green) over time (n=9). Gray and dark

Development • Advance article

green dotted lines denote τ_{area} and τ_{outer_MyoII} (the time when the cell started to accumulate MyoII with higher rate), respectively. (c-c') Confocal images of wild-type pupa expressing MyoII::GFP only in LECs, and MyoII::mCherry ubiquitously (Movie 11). (c) The double-arrow indicates MyoII accumulation in histoblasts attached to the apoptotic LEC. (c') MyoII::GFP images. Arrows represent the region where MyoII intensity in the apoptotic cell was analyzed. (d) Graphs plotting the normalized apical area (gray) and MyoII intensity (light green) of an apoptotic cell (n=8). Gray and green dotted lines denote τ_{area} and τ_{inner_MyoII} (the time when the cell started to accumulate MyoII at a higher rate), respectively. (e) Time delays between τ_{area} and either τ_{Inner_MyoII} (n=8) or τ_{Outer_MyoII} (n=9). *: $P<0.05$. Average values of data are shown as thick horizontal lines. Apoptotic LECs are highlighted by filled circles. Error bars indicate SEM. Scale bars, 20μm.

Development • Advance article

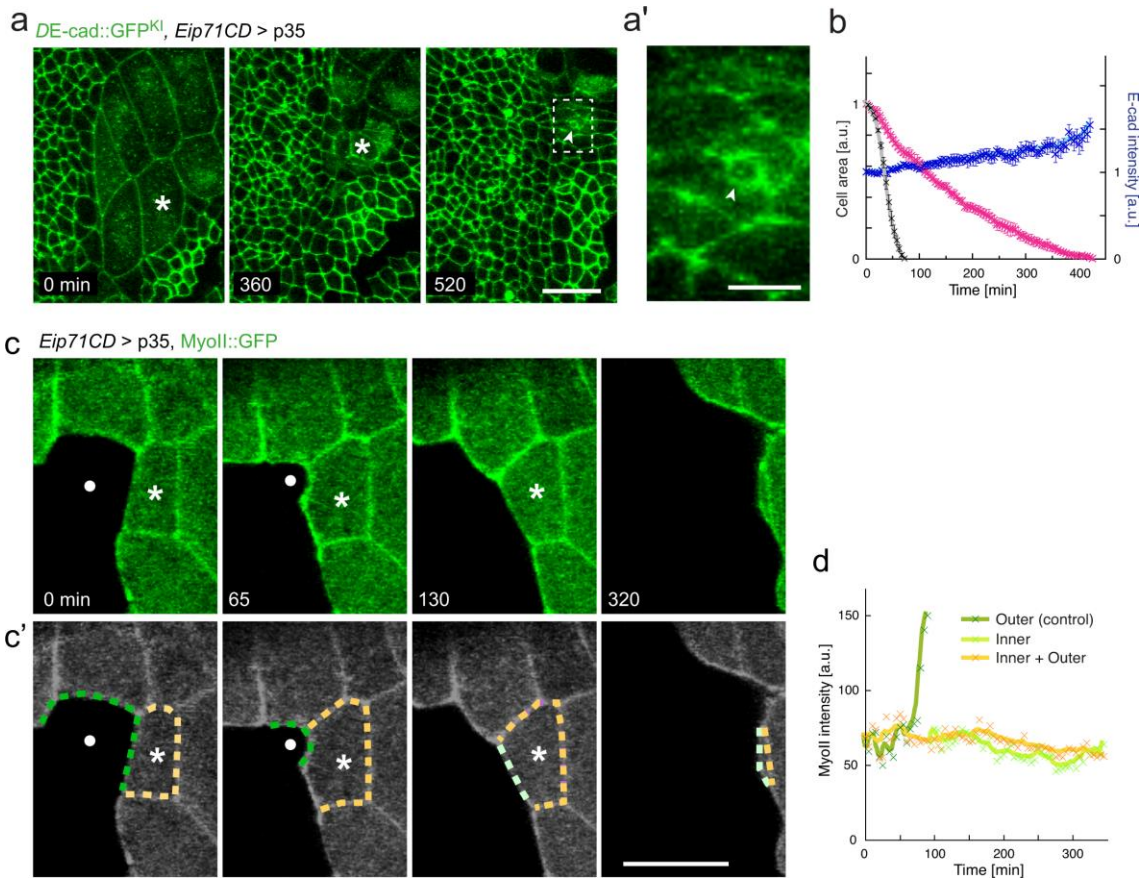


Fig. 5. Extrusion of LECs expressing caspase inhibitor p35 is distinct from that of wild-type LECs.

(a) Confocal images of pupa expressing caspase inhibitor p35 only in LECs, and *D*E-cad::GFP^{KI} ubiquitously (Movie 12). (a') High magnification of the dotted region depicted in (a). (b) Graphs plotting normalized cell apical area (pink) and E-cad level (blue) of extruding p35 expressing LECs over time (n=7). Error bars indicate SEM. Normalized apical cell area of wild-type apoptotic cells (gray, n=20) is shown for comparison. (c)

Development • Advance article

Confocal images of pupa expressing caspase inhibitor p35 and MyoII::GFP only in LECs. An extruding p35 positive LEC is highlighted with asterisks, wild-type apoptotic cell not expressing p35 and MyoII::GFP is highlighted by filled circle. (c') Dashed lines denote where MyoII intensity was analyzed in (c). Dark green lines highlighting the cell boundaries of LECs next to wild-type apoptotic LEC (filled circle), which represent the outer ring. Orange lines highlighting the cell boundaries shared by both p35 positive delaminating LEC (asterisk) and non-delaminating LECs. Light green lines highlighting the cell boundaries of p35 positive delaminating LEC (asterisk). Imaging started at 0min. Scale bars, 20μm (a, c') and 10μm (a'). (d) Graphs plotting MyoII intensities along three different lines shown in (c') over time.

Development • Advance article

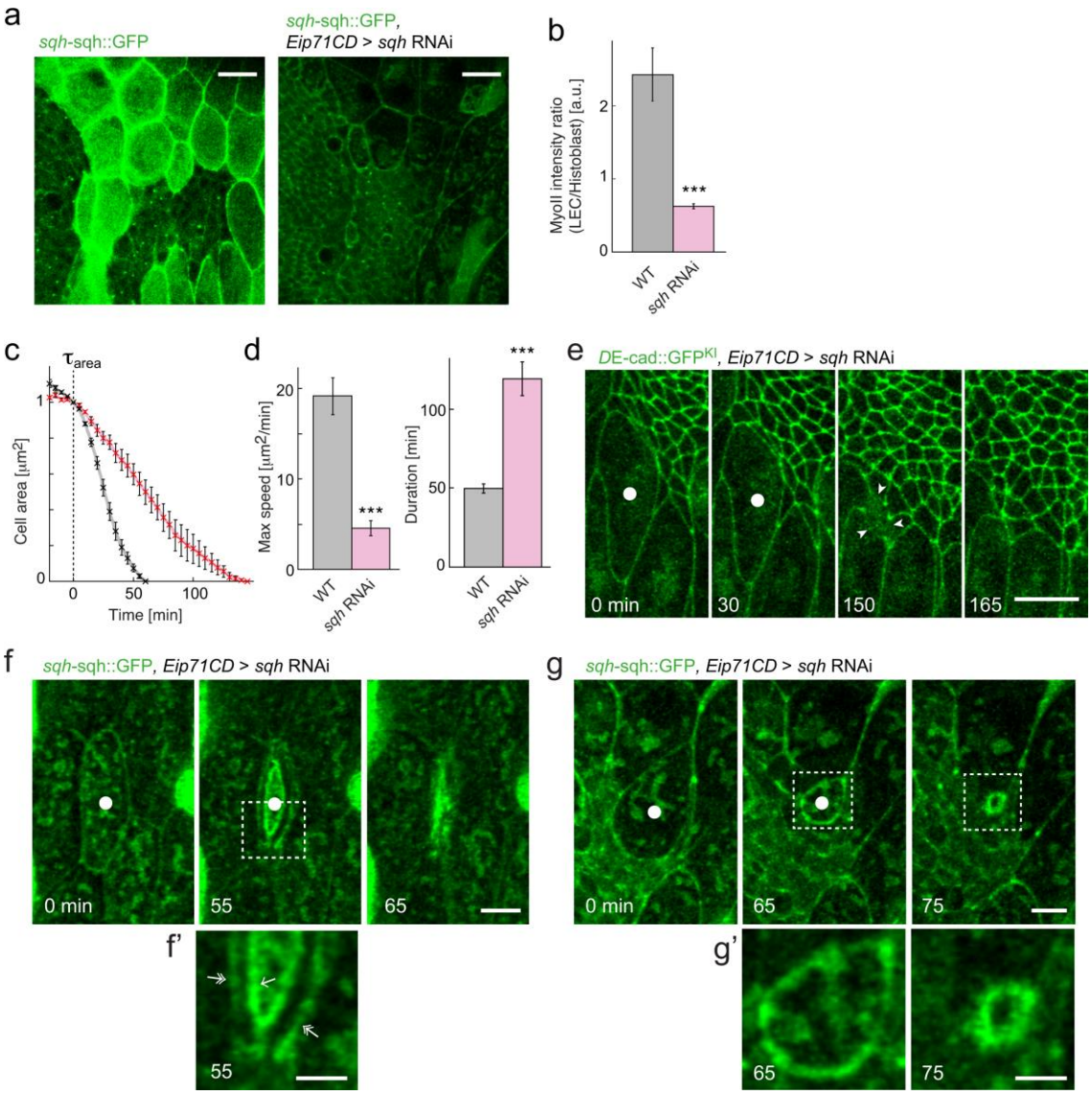


Fig. 6. Apoptotic cell extrusion in *sqh*-RNAi expressing LECs.

(a) Confocal images of wild-type pupa expressing MyoII::GFP ubiquitously (left) and pupa expressing *sqh*-RNAi only in LECs and MyoII::GFP ubiquitously (right). The contrast of

Development • Advance article

the images were adjusted so that the fluorescence intensity of histoblasts became equivalent. (b) Statistical comparison of the ratio of MyoII intensity between LECs and histoblasts. Gray and light red bars denote the mean values from wild-type and *sqh*-RNAi expressing LECs, respectively (n=6 and 7 pupae). Each ratio was calculated based on the average of 20 cell boundaries of LECs and histoblasts from an image. (c) Graphs plotting the normalized apical cell area of wild-type (gray, n=20) and *sqh*-RNAi positive (pink, n=5) apoptotic cells over time. τ_{area} denotes the time when the cell started to constrict with higher speed. Error bars indicate SEM. (d) Statistical comparison of the maximum speed of apical constriction (left) and the duration from τ_{area} to the completion of apical constriction (right). Gray and light red bars denote the mean values from wild-type and *sqh*-RNAi positive LECs, respectively (n=20 and 5). (e-g) Confocal images of pupa expressing *sqh*-RNAi only in LECs, and *D*E-cad::GFP^{KI} (e) or MyoII::GFP (f, g) ubiquitously. (e) A cell undergoes apoptosis and shows a reduction of E-cad levels (arrowheads) (Movie 14). (f, g) Confocal images of apoptotic cells with the space between MyoII cables (f) and without the space (g). (f', g') High magnification of the dotted region depicted in (f) and (g). Arrow and double-arrow in f' shows the myosin in an apoptotic cell and in neighboring cells, respectively. Imaging started at 0 min. Extruding *sqh*-RNAi positive LECs are highlighted by filled circles. ***: P<0.001. Scale bars, 20μm (a), 10μm (e-g) and 5μm (f', g').

Development • Advance article

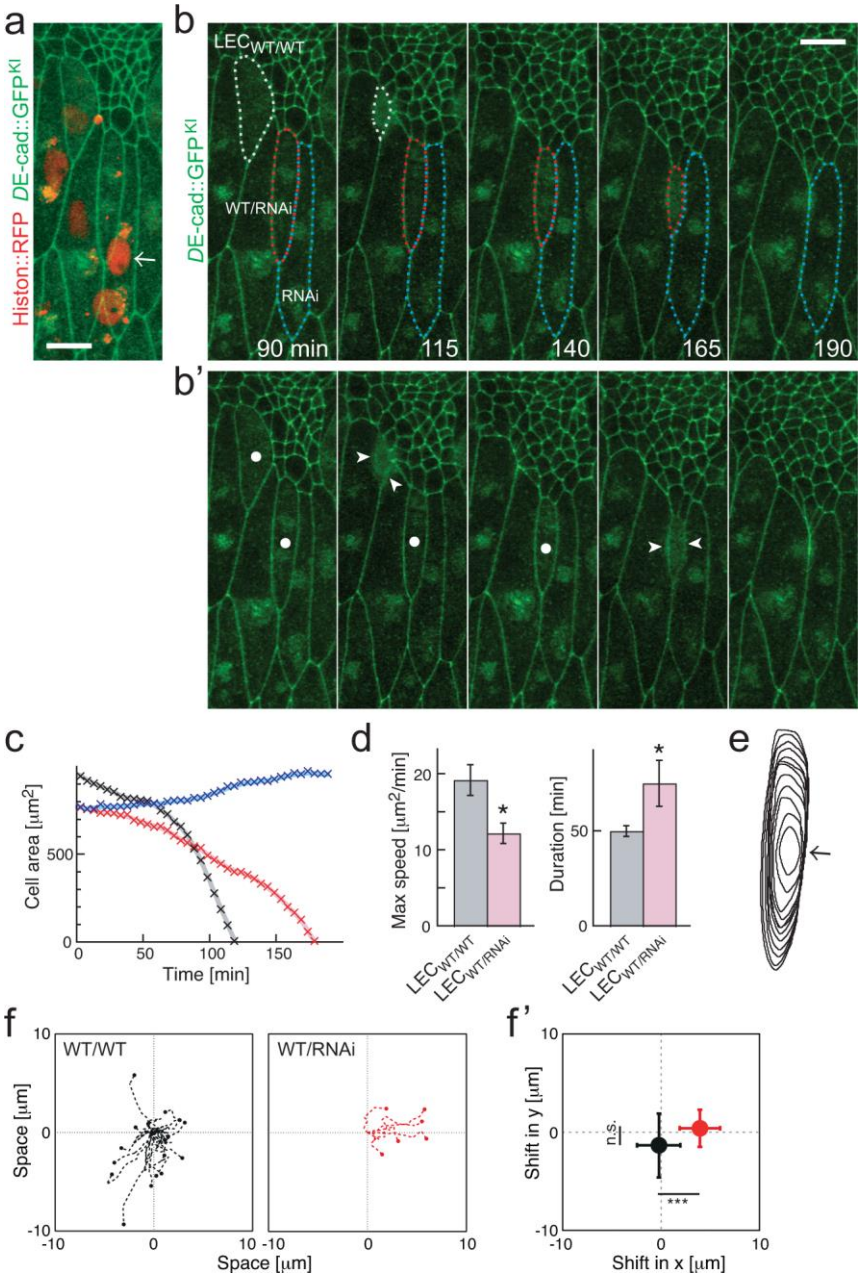


Fig. 7. Clonal disruption of MyoII in neighboring cells compromises apoptotic cell extrusion.

(a) Confocal images of pupa expressing *sqh*-RNAi to a subset of LECs. LECs with bright

Development • Advance article

(two copies of) Histone::RFP represent LECs expressing *sqh*-RNAi (white arrow), and is distinct from the control cells, which either lacked Histone-RFP, or expressed only a single copy. The pupa also expresses *D*E-cad::GFP^{KI}. (b, b') Stills from a time-lapse movie of the same pupa in (a) (Movie 15). (b) The cell highlighted with a blue dotted line is an LEC expressing *sqh*-RNAi (LEC_{RNAi}). The cell highlighted with a red dotted line is a wild-type LEC next to an RNAi positive LEC ($LEC_{WT/RNAi}$). The cell highlighted with a white dotted line is a wild-type LEC surrounded by wild-type histoblasts and LECs ($LEC_{WT/WT}$). The genotype of 3 different cells can be found in Materials and Methods. (b') Both $LEC_{WT/RNAi}$ and $LEC_{WT/WT}$ undergo apoptosis and show the reduction of E-cad levels (arrowheads). (c) Graphs showing the apical cell area of the apoptotic $LEC_{WT/WT}$ (black), apoptotic $LEC_{WT/RNAi}$ (red) and neighboring LEC_{RNAi} (blue). (d) Statistical comparison of the maximum speed of apical constriction and the duration from τ_{area} to the completion of apical constriction. Gray and light red bars denote the mean values from $LEC_{WT/WT}$ and $LEC_{WT/RNAi}$, respectively (n=58 and 6). (e) Contour plots showing the apical cell shape change of the apoptotic $LEC_{WT/RNAi}$ highlighted in (b) over time. The constriction appears to be biased toward the RNAi positive cell (arrow). (f) Trajectory of the centroid of apoptotic cell shape after τ_{area}. Trajectories of $LEC_{WT/WT}$ cells (n=20) and $LEC_{WT/RNAi}$ cells (n=6) are shown in black and red, respectively. For the analysis of $LEC_{WT/RNAi}$ cells, the images were rotated so that the RNAi positive cell was placed to the right of the apoptotic cell. (f') Statistical comparison of the end point of trajectory shown in f. Error bars indicate SEM. *: $P<0.05$, ***: $P<0.001$, n.s.: Not significant. Scale bars, 20μm.

Development • Advance article

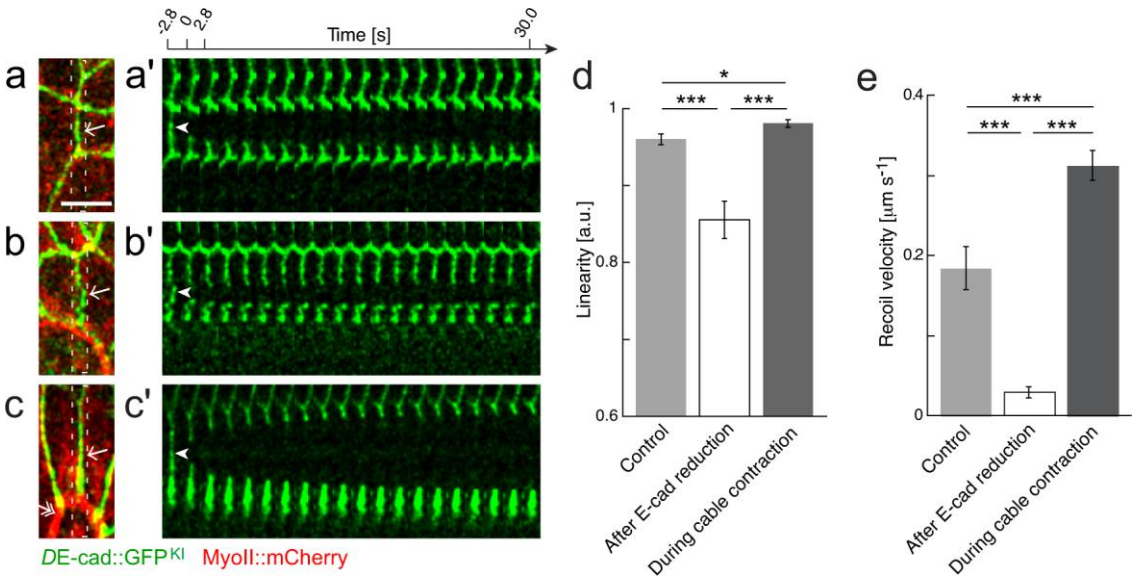


Fig. 8. Tissue tension release and reshape after reduction of E-cad levels. (a-c) Confocal images of wild-type pupae expressing *D*E-cad::GFP^{KI} and MyoII::mCherry ubiquitously highlighting the histoblast cell boundaries connected to the apoptotic LEC (arrows) before laser ablation. (a'-c') Kymographs generated from the white boxed regions in a-c, showing the dynamics of the cell boundaries after ablation (Movie 16). The laser ablations (arrowheads) were performed in three different stages of apoptotic cell extrusion: before reduction of E-cad levels (a-a'); right after reduction (b-b'); and during neighboring actomyosin cable (double-arrow in c) contraction (c-c'). Scale bar, 5μm. Statistical comparison of the cell boundary linearities (d) and the recoil velocities (e) at each stage of cell extrusion shown in a-c. n=17, 12 and 27 for control, after reduction, and, during cable contraction, respectively. Error bars indicate SEM. *: P<0.05, ***: P<0.001.

Development • Advance article

Supplemental Information

Supplemental Figures

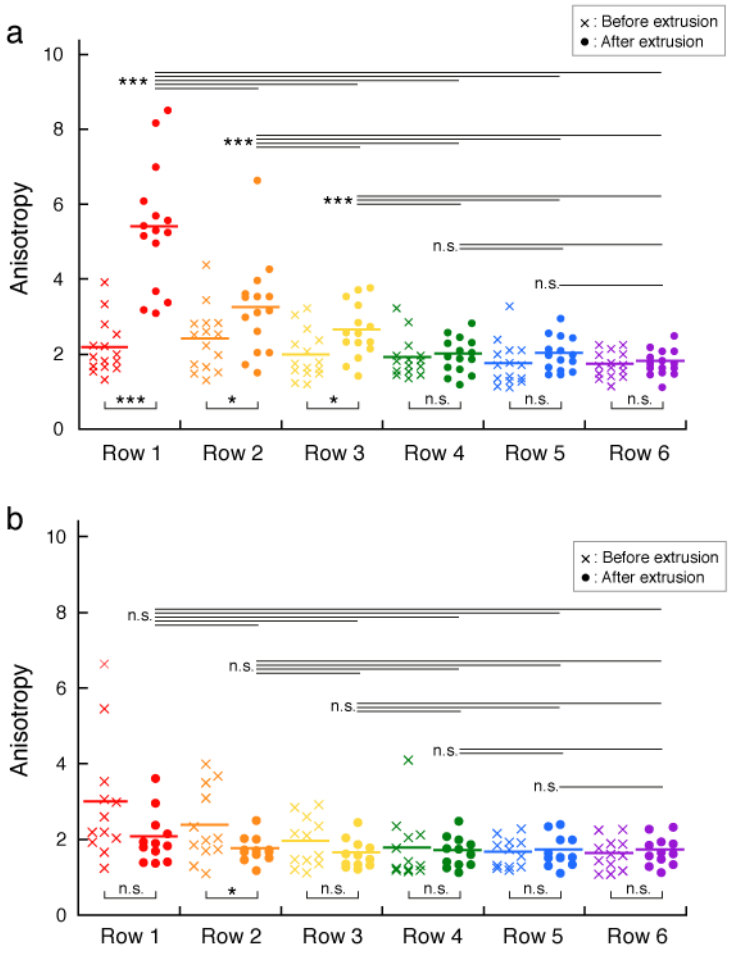


Fig. S1. Quantification of cell shape deformation of histoblasts upon extrusion of boundary LEC. (a and b) Plots of anisotropy of cell shape (Supplemental Materials and Methods) before (crosses) and after (filled circles) the boundary cell extrusions, as a function of distance (i.e., number of rows) from the boundary LECs (n=15 from 3 pupae). Data from wild-type pupae (a) and pupa expressing sqh-RNAi only in LECs (b). *: $p<0.05$, ***: $p<0.001$, n.s.: no significance.

Development • Supplementary information

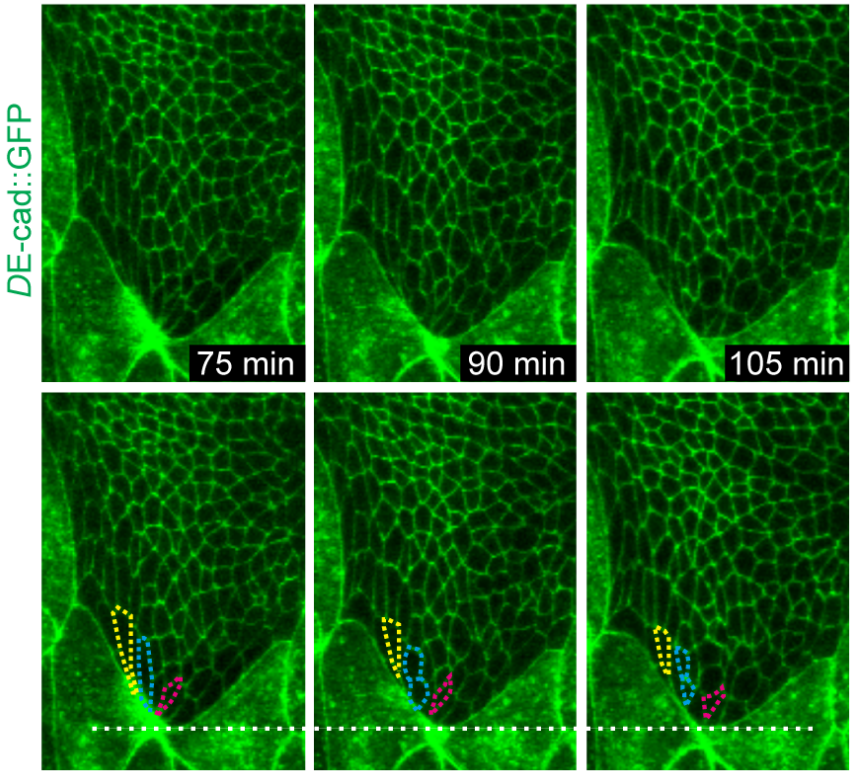


Fig. S2. Fate of the elongated histoblasts after the completion of apical constriction of apoptotic LEC. Confocal fluorescence images of wild type pupa expressing *D*E-cad::GFP, showing the fate of the elongated histoblasts presented in Fig. 1 b and 1c. The first time frame (denoted as 75 min) is the same image as the last frame of Fig. 1b (denoted as 75 min). The elongated histoblasts underwent either cell division (highlighted with blue dotted line) or cell-cell junction remodeling (highlighted with yellow and red dotted lines) after the completion of cell extrusion. White dotted line denotes the edge of the histoblasts.

Development • Supplementary information

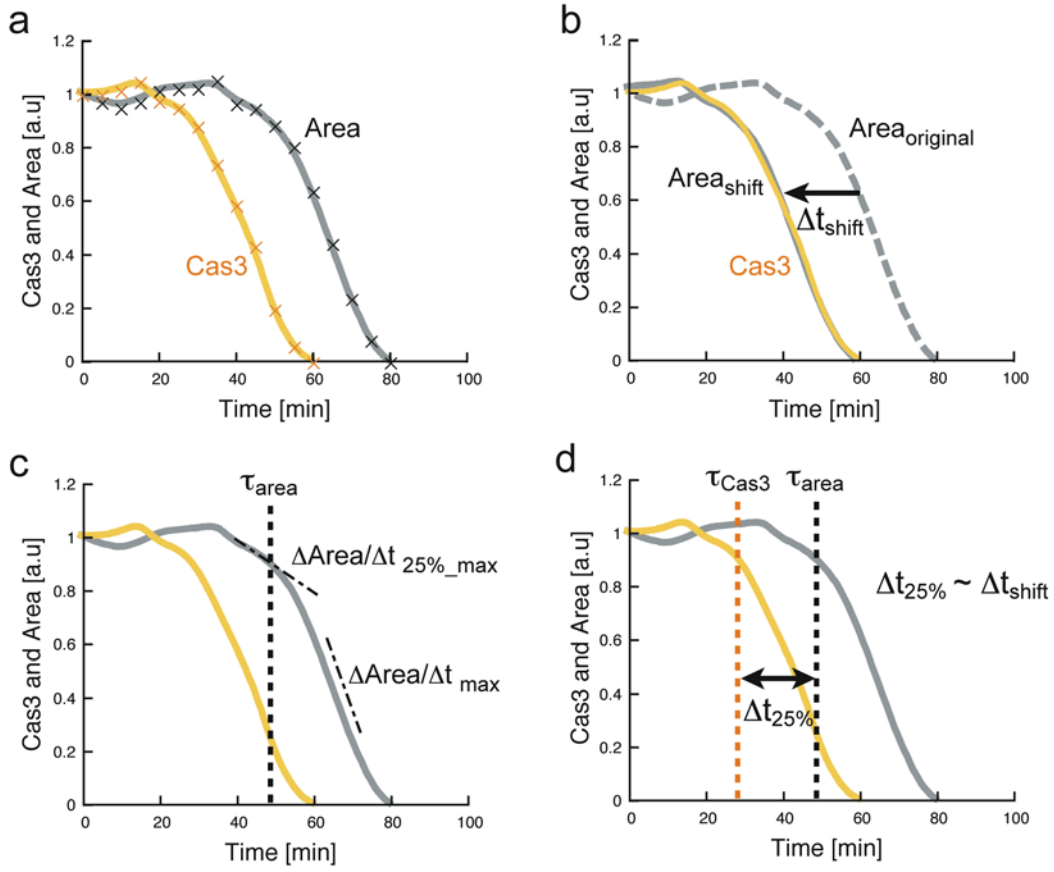


Fig. S3. Determination of transition time. Refer to Materials and methods for more detail. (a) Graphs showing the normalized apical area (gray line) and caspase-3 activity (orange) of apoptotic cell over time. (b) Original Area graph ($Area_{original}$, gray dotted line) was shifted by Δt_{shift} so that the difference between shifted area ($Area_{shift}$, gray solid line) and caspase-3 data (orange line) is minimized. Note gray and orange solid lines are overlapping each other. (c) Transition time of cell area, τ_{area} was determined as the time when the derivative of the graph ($\Delta Area/\Delta t$) reached to 25% of the maximum slope ($\Delta Area/\Delta t_{max}$). (d) The time delay between the initiation of apical constriction and caspase-3 activation measured by 25% of maximum slope, $\Delta t_{25\%} = |\tau_{area} - \tau_{Cas3}|$, was consistent to Δt_{shift}.

Development • Supplementary information

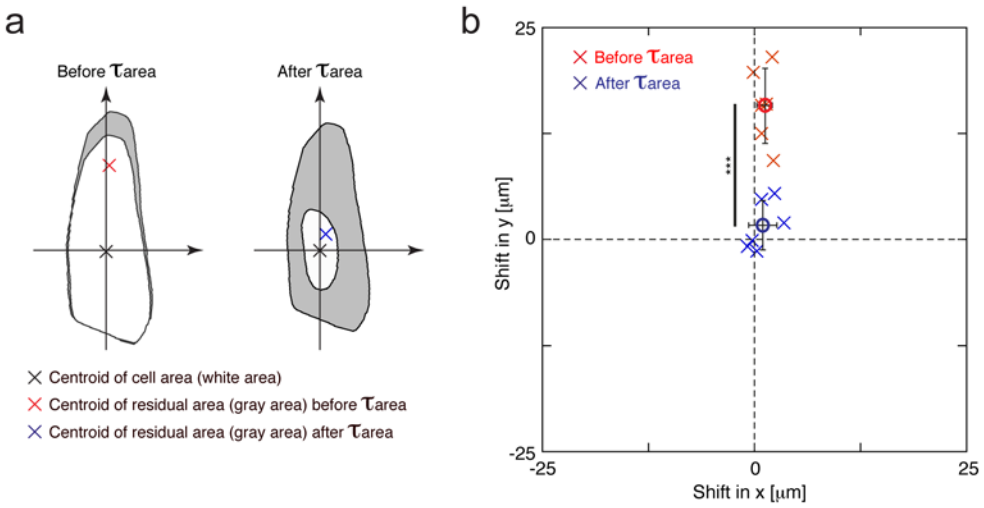


Fig. S4. Quantitative analyses of the deformation in the shape of extruding LECs. (a) Two contour plots showing the cell shape of different time points (25 min apart) for before (left) and after (right) τ_{area}. Black cross denotes the centroid of the cell area at later time point (white in the figure). Red and blue crosses denote the centroid of residual area (difrence between two contour plots, gray in the figure) at before and after τ_{area}, respectively. (b) Summary of 6 data. Open circles and error bars represent the average values and the STDEV, respectively. ***: $p<0.001$.

Development • Supplementary information

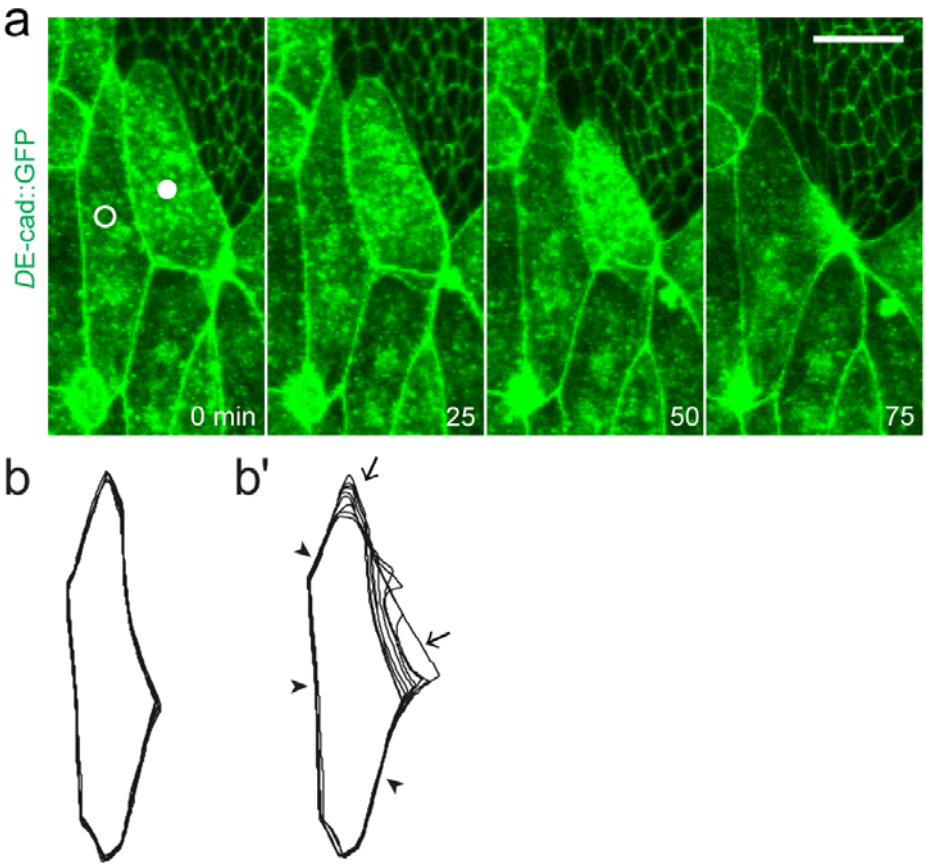


Fig. S5. Kinematics of a LEC next to an apoptotic LEC. Confocal fluorescence images of wild type pupa expressing *D*E-cad::GFP, showing the cell shape deformation of a non-dying LEC (highlighted by open circle), which is next to an apoptotic cell (highlighted by filled circle) and same cell as shown in Fig. 1b. Time stamps denote the same time as shown in Fig. 1b. Scale bar, 20 µm. (b) Contour plots showing the cell shape deformation of the non-dying LEC highlighted in (a) prior to τ_{area} of the apoptotic cell, showing a little deformation. (b') Contour plots of the non-apoptotic LEC from τ_{area} onwards. The cell deformation is local. Arrow indicates the region with major deformation. Arrowheads highlight the cell boundary with little or no deformation.

Development • Supplementary information

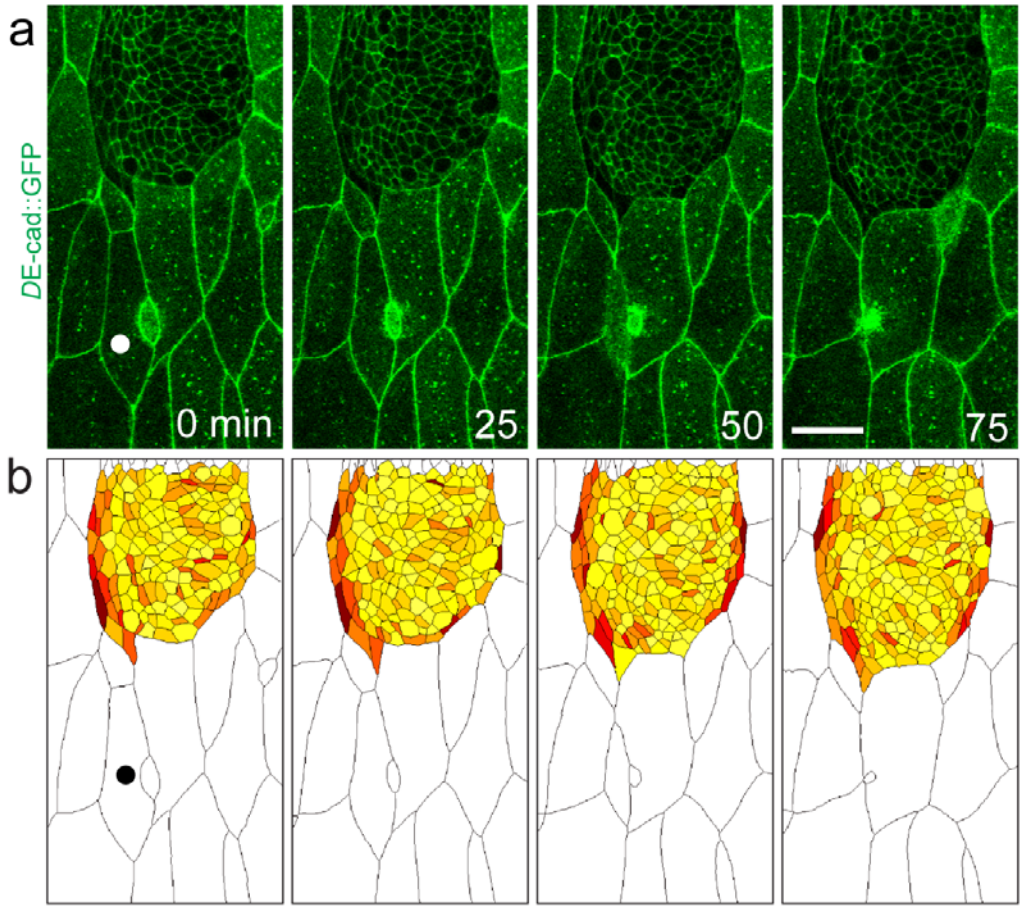


Fig. S6. Mechanical impact of non-boundary LEC apoptosis. (a) Confocal fluorescence images of wild type pupa expressing *D*E-cad::GFP. Non-boundary LEC (i.e., one LEC away from histoblast) is highlighted by filled circles. Scale bars, 50 μm. (b) Color-enhanced reproduction of the confocal images from (a). Colors demote the anisotropy of the cell shape: The darker color represent more elongated histoblast cells (same as Fig. 1c). The color of the histoblasts did not change as much as the case of boundary LEC. Scale bar, 20 μm.

Development • Supplementary information

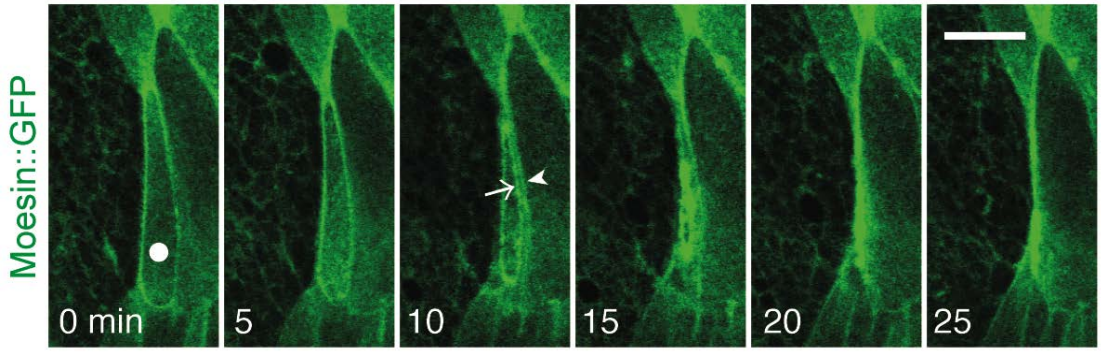


Fig. S7. Actin distribution around the periphery of apoptotic LEC shows two actin cable-like structures. Confocal fluorescence images of wild type pupa expressing Moesin::GFP. Apoptotic LECs are highlighted by filled circles. Arrow and arrowhead show the actin accumulation in the apoptotic LEC and the neighboring non-apoptotic LECs, respectively. Scale bar, 20 μm.

Development • Supplementary information

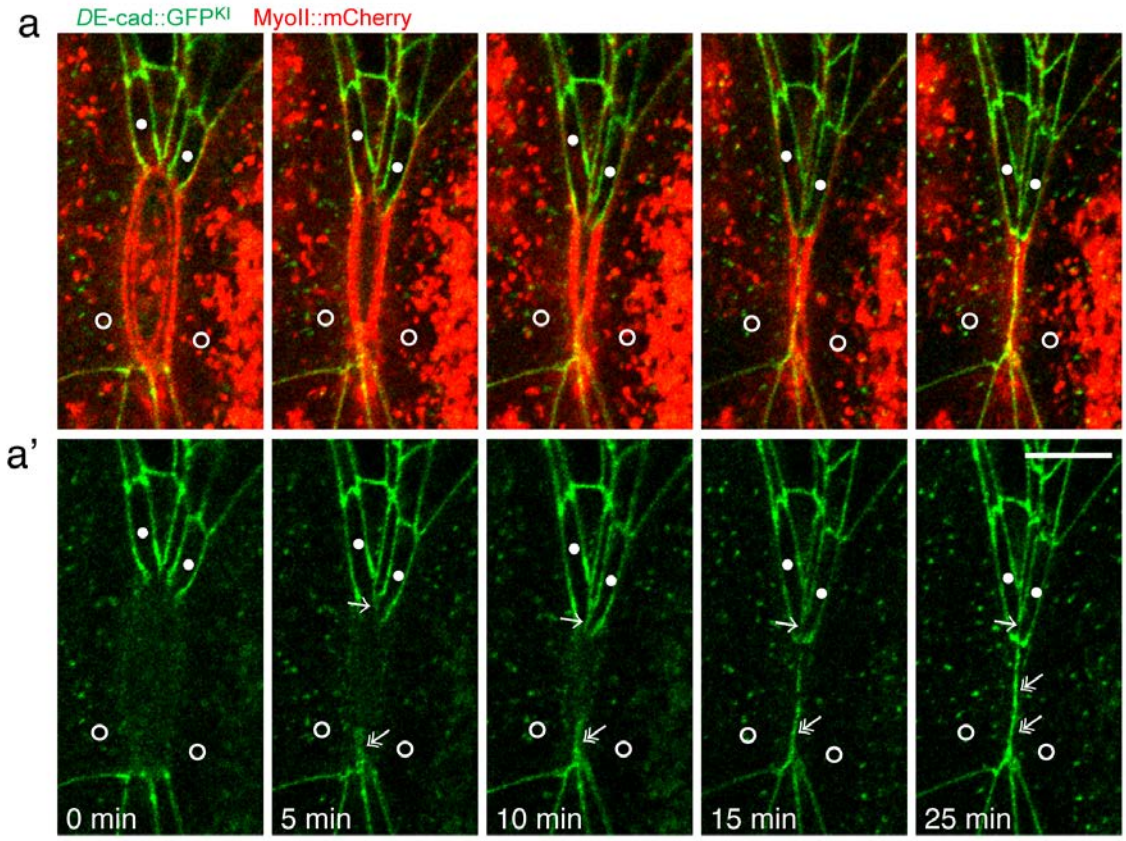


Fig. S8. Formation of *de novo* AJs between the non-apoptotic neighboring cells. Confocal fluorescence images of wild type pupae expressing *D*E-cad::GFP and MyoII::mCherry. Two pairs of neighboring cells (filled and open circles) form *de novo* AJs before the completion of apoptotic cell extrusion (arrows and doublearrows). Scale bar, 10 μm.

Development • Supplementary information

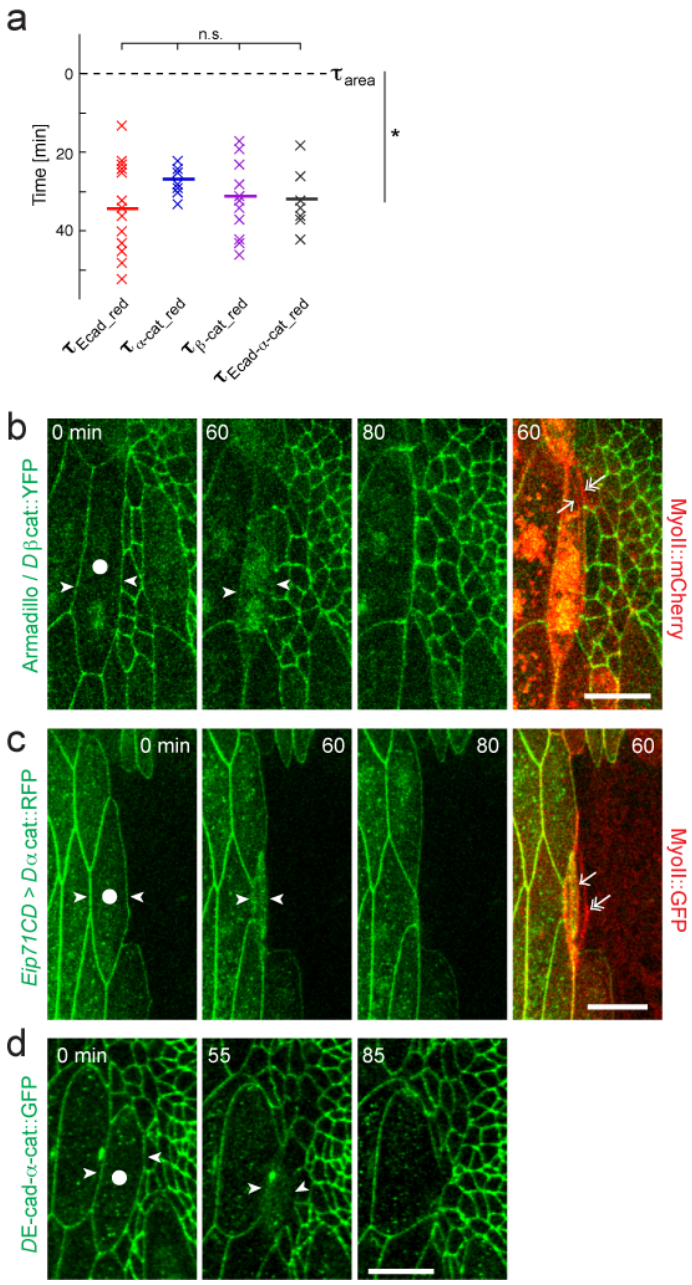


Fig. S9. Reduction of the level of AJ components during apoptosis. (a) Time delays of the reduction of AJ components (τ_{Ecad_red}, $\tau_{\alpha\text{-}cat_red}$, $\tau_{\beta\text{-}cat_red}$, and $\tau_{Ecad\text{-}\alpha\text{-}cat_red}$) using area transition τ_{area} as a reference (*: $P < 0.05$, n.s.: Not significant). n=13, 9, 12, and 7 for τ_{Ecad_red}, $\tau_{\alpha\text{-}cat_red}$, $\tau_{\beta\text{-}cat_red}$, and $\tau_{Ecad\text{-}\alpha\text{-}cat_red}$, respectively. Average values are shown as thick horizontal lines. (b and c) Confocal fluorescence images of wild type pupa expressing *D*β-cat::YFP and MyoII::mCherry (b, Movie 7) or pupa expressing α-cat::RFP only in LECs and MyoII::GFP ubiquitously (c, Movie 8). (d) Confocal fluorescence images of pupa expressing GFP tagged fusion protein that the C-terminal domain of E-cad was replaced by an α-cat protein lacking the N-terminal domain (*DE*-cad-α-cat::GFP). Apoptotic LECs are highlighted by filled circles. Arrowheads shows the dissociation of fluorescence signal. Arrows and double arrows denote the myosin in the apoptotic LEC and the neighboring cells, respectively. Scale bars, 20 μm.

Development • Supplementary information

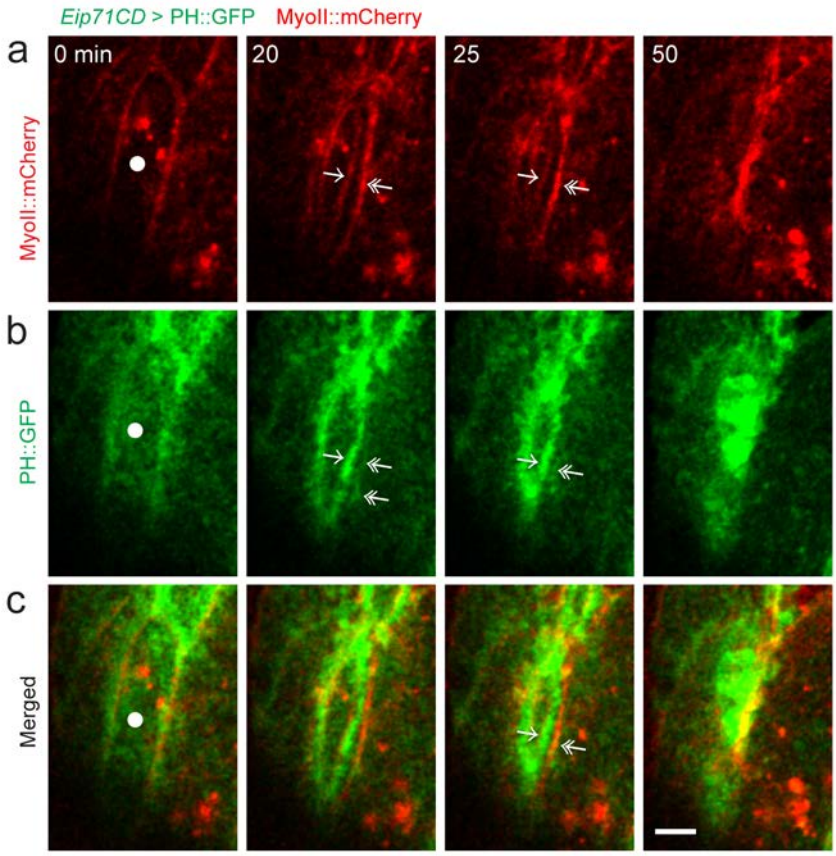


Fig. S10. AJ disengagement upon apoptosis. Confocal fluorescence images of wild type pupa expressing the plasma membrane markers PH::GFP in LECs, and MyoII::mCherry ubiquitously, highlighting the plasma membranes of apoptotic (arrow) and neighboring (double arrows) cells detach once the separation of the two myosin cables become apparent. Same data as shown in Fig. 3g. Scale bar, 20 μm.

Development • Supplementary information

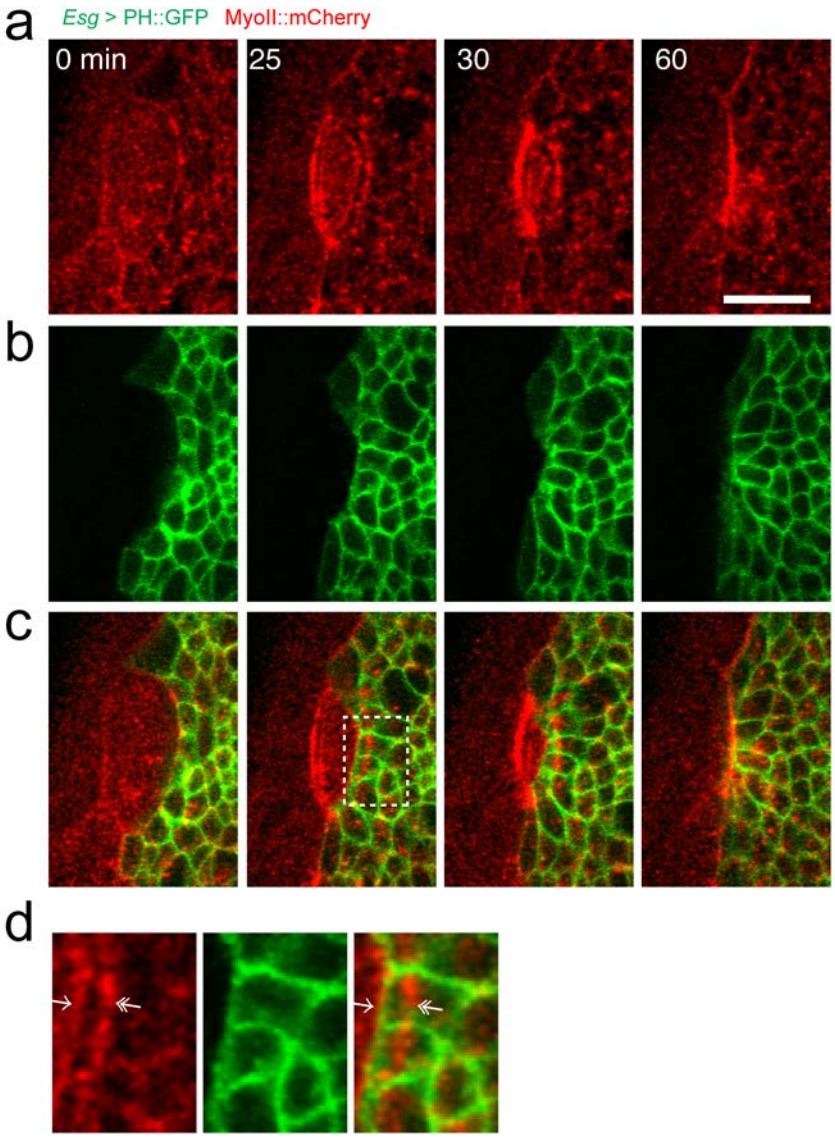


Fig. S11. AJ non-disengagement upon apoptosis. (a-c) Confocal fluorescence images of wild type pupa expressing the plasma membrane markers PH::GFP only in the histoblasts, and MyoII::mCherry ubiquitously. (d) High magnification of the dotted region depicted in (c), highlighting the myosin cable in the apoptotic cell (arrow) and the edge of the histoblast membrane are closely juxtaposed each other. Moreover, the myosin cable in the neighboring cells (double arrowheads) is away from the membrane. Scale bar, 20 μm.

Development • Supplementary information

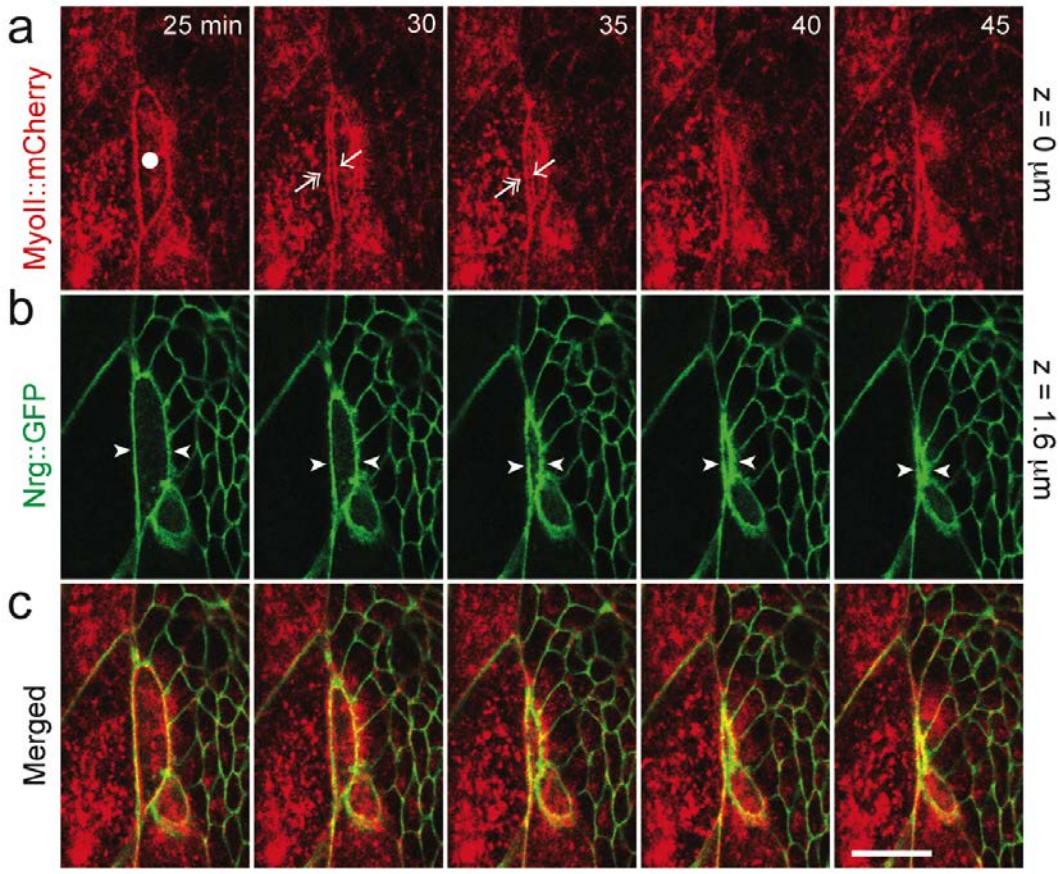


Fig. S12. Dynamics of septate junction (SJ) during LEC apoptosis.
(a-c) Confocal fluorescence images of wild type pupa expressing the septate junction marker Nrg::GFP and MyoII::Cherry (Movie 9). Imaging started at 0 min. (a) MyoII images from a z-section at AJ. Apoptotic LEC is highlighted by filled circles. Arrows and double arrows show the MyoII accumulation in the apoptotic LEC and the neighboring LECs, respectively. (b) Images of the septate junction from a z-section 1.6 μm below AJ. Arrowheads indicate the septate junction is not compromised during the apical constriction of the apoptotic cell. (c) Merged image. Scale bar, 20 μm.

Development • Supplementary information

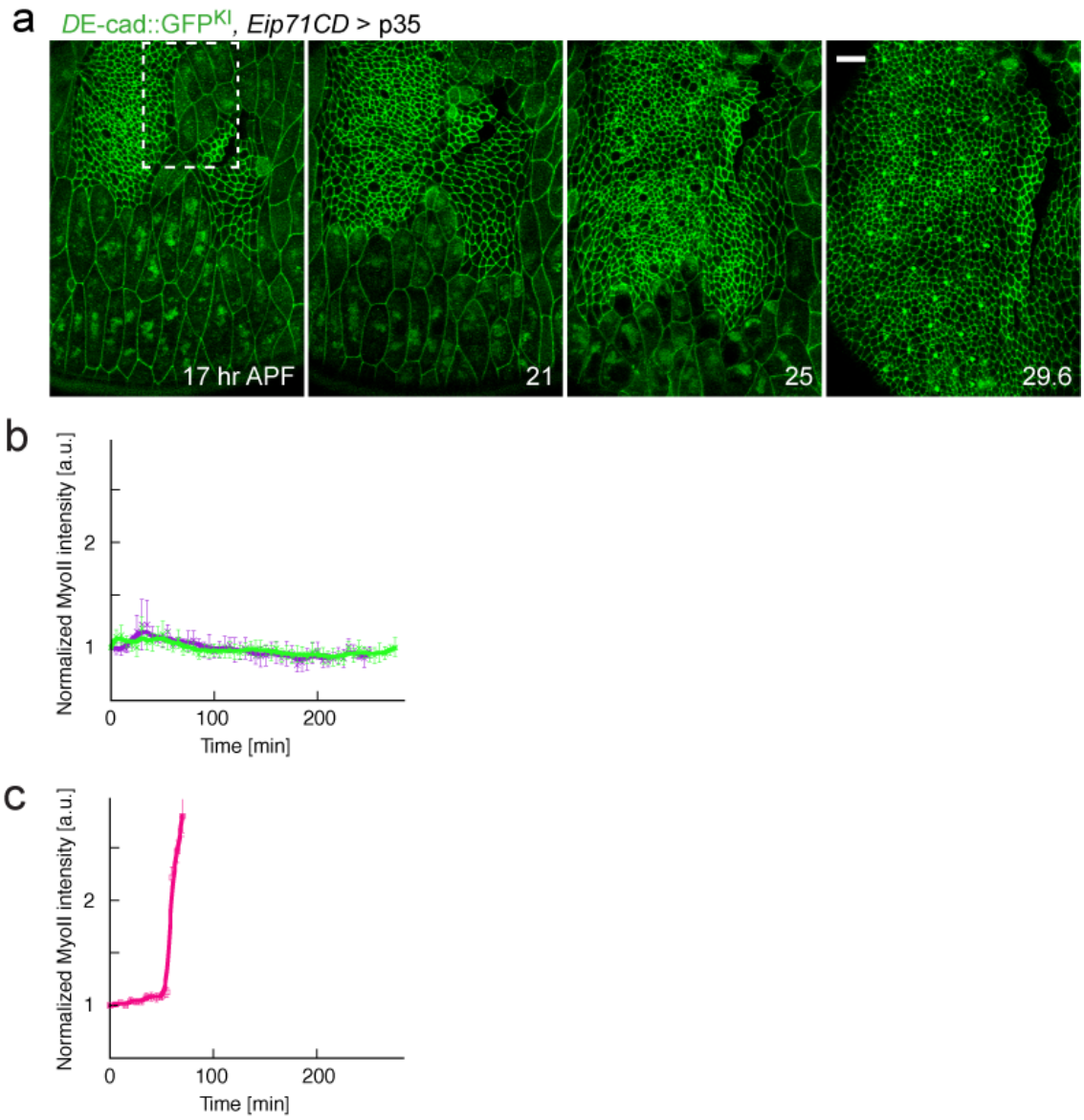


Fig. S13. Extrusion of LECs expressing caspase inhibitor. (a) Confocal fluorescence images of pupa expressing caspase inhibitor p35 only in LECs, and *D*E-cad::GFP^{KI} ubiquitously, showing anterior and posterior dorsal histoblast nests and LECs at 17, 21, 25, and 29.6 hours APF. White dotted region represent the field shown in Fig. 5a. Scale bars, 20 μm. (b) Graphs plotting normalized MyoII intensity of extruding cell (green, n=5) and of the summation of extruding cell and neighboring cell (purple, n=7) over time. (c) Graphs plotting normalized MyoII intensity of the summation of apoptotic cell and neighboring cell in wild-type pupae (pink, n=6) over time. Error bars indicate SEM.

Development • Supplementary information

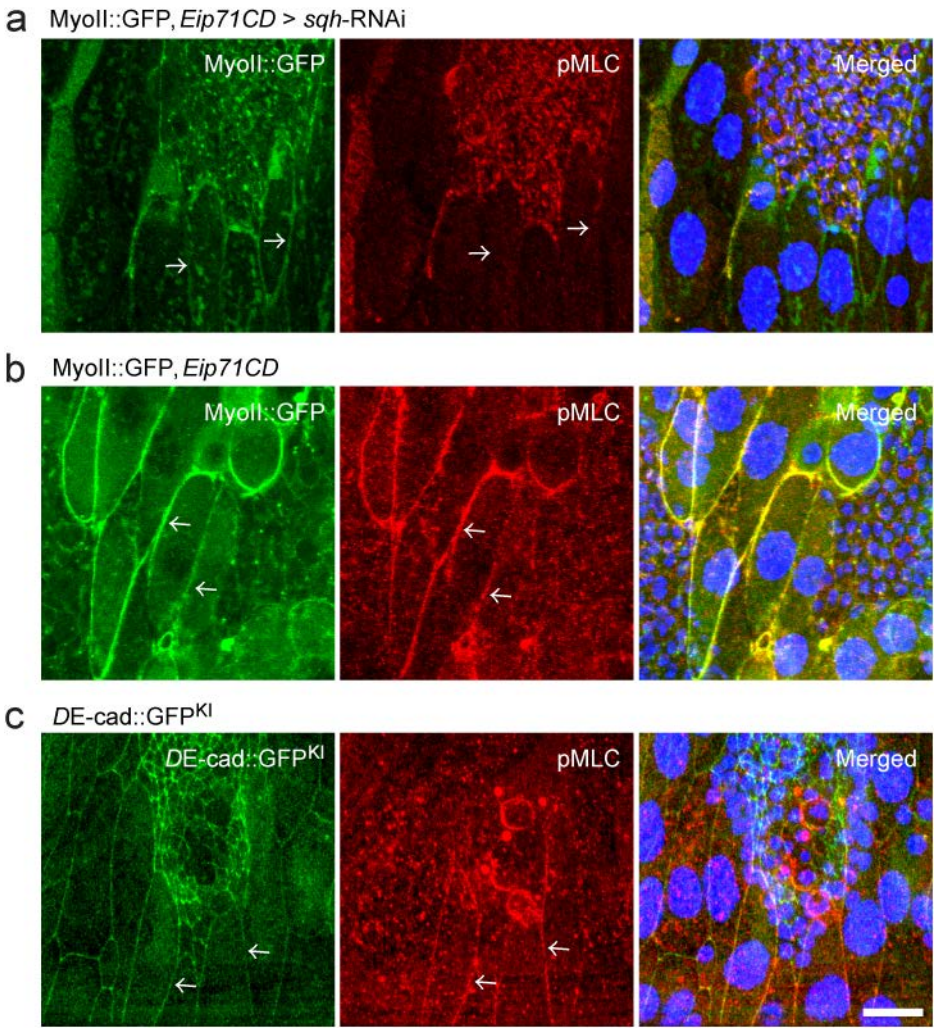


Fig. S14. Level of phosphorylated myosin regulatory light chain in different pupae. (a-c) Confocal fluorescence images of pupae stained with phosphorylated myosin regulatory light chain (pMLC, red) and DAPI (blue). (a) Images of pupa expressing sqh-RNAi only in LECs, and MyoII::GFP ubiquitously. (b and c) Images of control pupa expressing MyoII::GFP (b) and *D*E-cad::GFP^{KI} (c), ubiquitously. The level of pMLC at cell boundaries (arrows) in sqh-RNAi expressing LECs is weaker than that of control LECs. Scale bar, 20 µm.

Development • Supplementary information

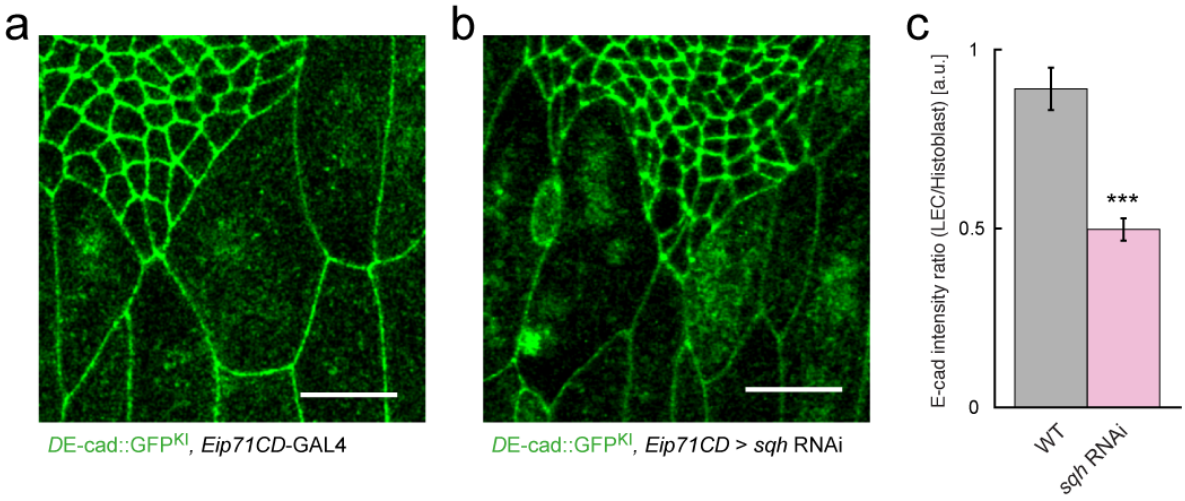


Fig. S15. Level of E-cad in LECs expressing *sqh*-RNAi.
(a, b) Confocal fluorescence images of wild-type pupa expressing *D*E-cad::GFP^{KI} ubiquitously (a) or pupa expressing *sqh*-RNAi only in LECs and *D*E-cad::GFP^{KI} ubiquitously (b). The contrast of the images were adjusted so that the fluorescence intensity of histoblasts became equivalent. No apoptotic cells are shown in both images. (c) Statistical comparison of the ratio of E-cad intensity between LEC and histoblast. Gray and light red bars denote the mean values from wild-type and sqh-RNAi expressing LECs, respectively (n=5 and 8). Each ratio was calculated based on the average of 20 cell boundaries of LECs and histoblast from an image. Scale bars, 20 μm

Development • Supplementary information

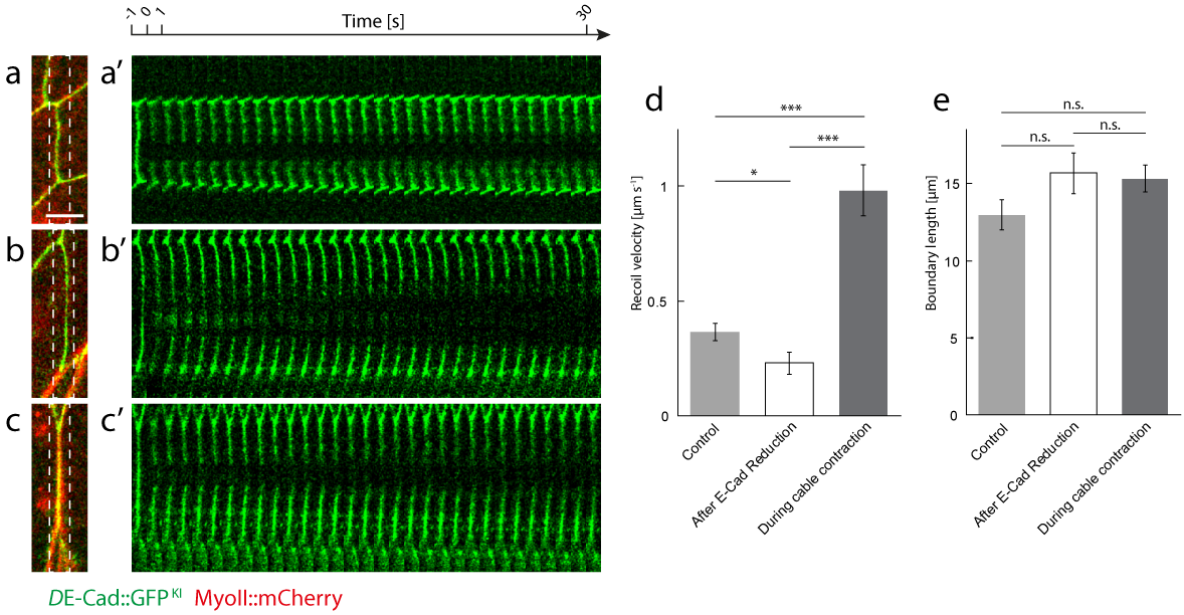


Fig. S16. Tissue tension release and reshape after reduction of E-cad levels in LECs. (a-c) Confocal fluorescence images of wild-type pupa expressing *D*E-cad::GFP^{KI} and MyoII::mCherry ubiquitously highlighting the LEC boundaries connected to the apoptotic LEC before ablation. (a'-c') Kymographs generated from the white boxed regions in a-c, showing the dynamics of the cell boundaries after ablation. The ablations were performed in three different stages of apoptotic cell extrusion: before reduction of E-cad levels (a and a'); right after reduction (b and b'); and during neighboring actomyosin cable (double-arrow in c) contraction (c and c'). Scale bar, 10 μm. Statistical comparison of the recoil velocities (d) and the length of cell boundary at laser ablation (e) at each stage of cell extrusion shown in a-c. n=16, 11 and 13 for control, after reduction, and, during cable contraction, respectively. Error bars indicate SEM. *: $P < 0.05$, ***: $P < 0.001$, n.s.: no significance.

Development • Supplementary information

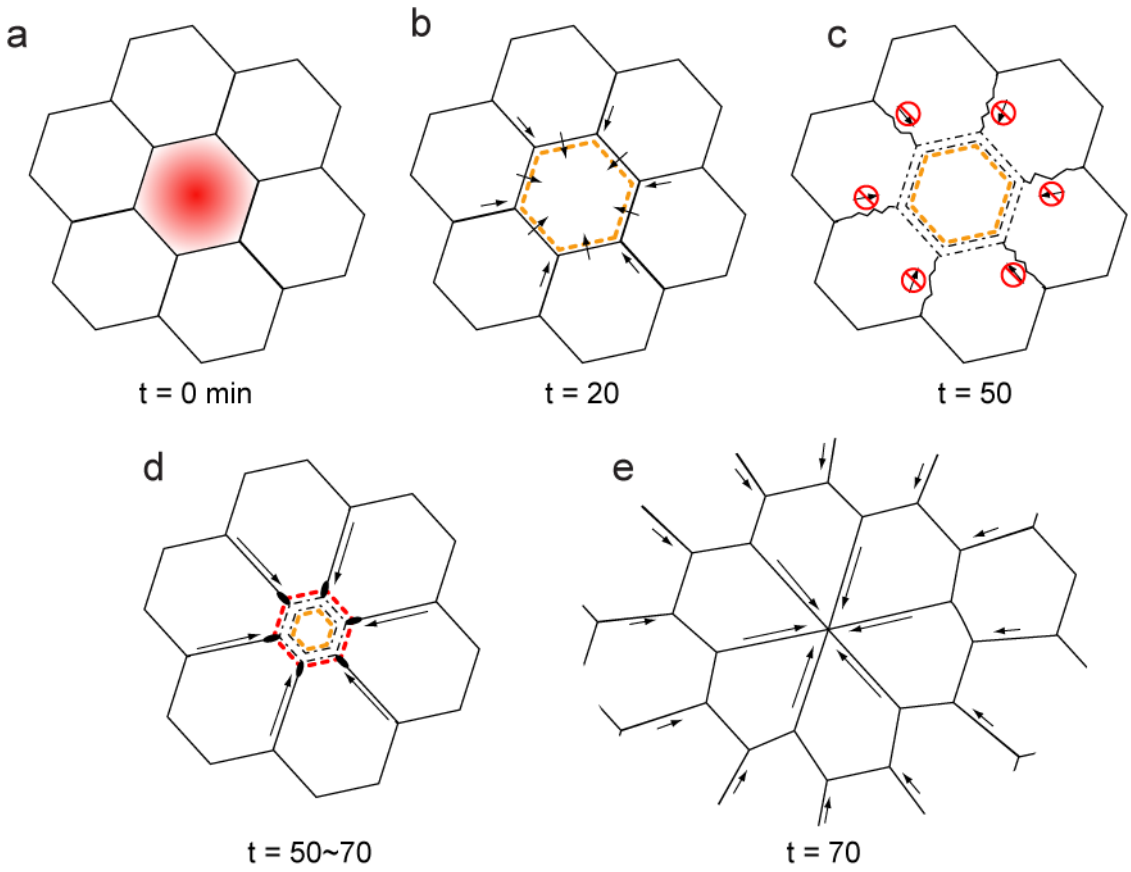


Fig. S17. A model of the progressive remodeling of AJ and tissue tension during apoptosis. Cartoons show the progression of apoptotic events with the top view at the AJ. Cell size and shape are not scale. (a) Caspase activation (set this time as t=0min). (b) Beginning of apical constriction and MyoII accumulation (orange dotted line) in the apoptotic cell (t=20min). The contraction of the actomyosin cable pulls the neighboring cells through the AJ (black arrows). (c) AJ disengagement (black dotted lines) and tension release (t=50min). (d) MyoII accumulation in neighboring non-apoptotic cells (red dotted lines). Contraction of supra-cellular actomyosin cables reshape the tissue tension (black arrows) (t=50-70min). (e) End of apical constriction. The propagation of mechanical force promotes tissue dynamics (black arrows) (t=70min).

Development • Supplementary information

Supplemental Experimental Procedures

Drosophila stocks and Genetics

Otherwise stated, fly stocks were obtained from the Bloomington Stock Center. The following lines were used: *ubi*-E-cad::GFP (H. Oda), Nrg::GFP (Kyoto Stock Center), moe::GFP (D. Kiehart), *ubi*-E-cad::GFP; *sqh*-*Sqh*-mCherry (A.C. Martin), Armadillo::YFP , and Knock-in alleles of *D*E-cad::GFP and *D*E-cad::mTomato (Huang et al., 2009). The following UAS and GAL4 were used to ectopically express the gene of interest: UAS-*sqh*::GFP (M. Affolter), UAS-α-catenin::RFP (K. Sugimura), UAS-*sqh*-RNAi (VDRC), UAS-SCAT3 (M. Miura), UAS-p35, *Esg*-GAL4, *Eip71CD*-GAL4, and *tsh*-GAL4. Live imaging of E-cad and caspase-3 sensor SCAT3 was carried out by crossing *tsh*-GAL4, UAS-SCAT3/CyO (M. Miura) with *D*E-cad::mTomato (Huang et al., 2009).
sqh-RNAi MARCM clones that were positively marked by the double copy of histone-RFP expression were recovered from neoFRT19A, *tubP*-Gal80, *hs*FLP; UAS-*sqh*-RNAi (male), and neoFRT19A, *ubi*-mRFP.nls; *ubi*-E-cad::GFP, *Eip71CD*-GAL4 (female). Mitotic clones were induced using the FLP-FRT technique by using the *hs*-FLP with heat shock for 50 min at 37°C in early embryos. The genotypes of three cells analyzed in Fig. 7b are, neoFRT19A, tubP-Gal80, hsFLP/neoFRT19A, ubi-mRFP.nls; UAS-sqh-RNAi/ DE-cad::GFP-KI, Eip71CD-GAL4; +/+ ($LEC_{WT/WT}$), neoFRT19A, tubP-Gal80, hsFLP/neoFRT19A, tubP-Gal80, hsFLP; UAS-sqh-RNAi/ DE-cad::GFP-KI, Eip71CD-GAL4; +/+ ($LEC_{WT/RNAi}$), and neoFRT19A, ubi-mRFP.nls/neoFRT19A, ubi-mRFP.nls; UAS-sqh-RNAi/ DE-cad::GFP-KI, Eip71CD-GAL4; +/+ (LEC_{RNAi}).

Sample preparation and Live Imaging

Staged pupae were collected, dissected, mounted and imaged as previously described (Ninov and Martin-Blanco, 2007). Z-stack images were captured every 1.6 µm along the apical-basal axis of the tissue at 5-minute intervals (except Fig. 3d at 2.5 minute interval) with Nikon A1R MP confocal microscope with a Apo 40X WI λ S DIC N2, N.A 1.25 objective, or Zeiss LSM 510 Meta Inverted confocal microscope with a LD C-Apo 40X, N.A 1.1 objective. All imaging was performed at room temperature.

Immunohistochemistry

Pupae were staged as described in (Ninov and Martin-Blanco, 2007), dissected and fixed following protocols described in (Wang and Yoder, 2011). DNA was stained with 4',6-diamidino-2-phenylindole (DAPI). Primary antibody anti-pMLC (Cell Signaling, #3671) was used with concentration 1/50. Secondary antibody conjugated with Alexa 546 (Life Technologies) was used.

Laser ablation

Laser ablation at histoblast was performed using a Leica TCS SP5 multi-photon confocal microscope with a 63×/1.4-0.6 HCX PL Apo objective. Ablation was carried out at the AJ plane with a multi-photon laser (Mai-Tai HP from Spectra Physics, CA, USA) set to 800 nm, with a laser power of 40% out of 2.8 Watt maximum output. Laser ablation of LECs was performed using a femtosecond laser (FP1030 from fianium, UK) interfaced to the Nikon A1R MP confocal microscope. A laser power was set to 140 mW at back aperture of the objective. More detail can be found in (Hara et al., 2016).

Development • Supplementary information

Cell shape anisotropy analysis

To measure the anisotropy of individual histoblast cell (Fig. 1c and Fig. S1), the z-projected E-cad::GFP time-lapse images were first segmented by Packing Analyzer V2.0 (Aigouy et al., 2010). The cell boundary data were subsequently analyzed with Matlab software (MathWorks, MA, USA). Segmented cell shapes were fitted by ellipse, which was optimized by maximizing the area overlap between a segmented cell shape and an ellipse. Anisotropy of the cell was defined as the ratio of minor and major axes of the fitting ellipse.

Caspase-3 activity analysis

To monitor caspase-3 activity (Fig. 2a and Movie 5), fly with FRET base caspase-3 sensor, SCAT3 (Nakajima et al., 2011, Takemoto et al., 2003) was used. A 405nm laser was used to excite ECFP and two fluorescence images (ECFP and Venus) were simultaneously captured. FRET ratio was calculated by taking the intensity ratio between the sum-intensity z-projected ECFP and Venus images. FRET ratio of an apoptotic LEC (Fig. 2c) was measured by averaging the FRET ratio within an apoptotic cell. The shape of an apoptotic cell was manually segmented from the sum-intensity z-projected Venus images over time by using ImageJ (Schneider et al., 2012).

Determination of the transition time

To measure the time delay between the beginning of apical constriction and caspase-3 activation (Fig. 2c), we first normalized the cell area and caspase-3 activity data to the value measured at time = 0 sec (Fig. S3a). The area data was shifted in time to minimize the difference between area and caspase-3 data (Fig. S3b). The shift was defined as Δt_{shift}.

To determine when the cell started to constrict with higher speed (τ_{area}) and when the cell started to activate its Cas-3 activity (τ_{Cas3}) without comparing the two graphs, we referred to the maximum derivative of each graphs. We defined τ_{area} as the time when the derivative of the graph reached to 25% of the maximum slope (Fig. S3c). Similarly, we defined τ_{Cas3}. The time delay between the initiation of apical constriction and caspase-3 activation measured by 25% of maximum slope, $\Delta t_{25\%} = |\tau_{area} - \tau_{Cas3}|$, was consistent to Δt_{shift} (Fig. S3d). With the other values, e.g., numbers between 10% and 40%, $|\tau_{area} - \tau_{Cas3}|$ was not as close to Δt_{shift} as 25%.

Same setting (25% of the maximum slope) was used to define the transition time not only for τ_{area} and τ_{Cas3}, but also for all the other data, for instance τ_{EcadKI}, τ_{outer_MyoII} and τ_{inner_MyoII}.

MyoII intensity analysis

To quantify the progression of MyoII accumulation in apoptotic LECs or neighboring cells, the average fluorescent intensity of MyoII::GFP signal either from histoblast that originally attached to apoptotic LEC (Fig. 4a') or solely originated from the cell periphery of apoptotic LECs (Fig. 4c') were measured. Images of sum-intensity z-projection (around AJ) of MyoII::GFP were analyzed over time. ROIs (see main text for more detail) to calculate the intensity were manually defined by the free-hand line tools of ImageJ. The total intensity along the line with thickness of 4 pixels (0.24 μm/pixel) was measured and divided by the length of the line.

Cell boundary linearity measurement

Linearity of the histoblast cell boundaries was calculated as a ratio of the two ends of boundary (measured by using ImageJ Straight Line tool) to the actual length of the histoblast cell boundary (measured by using ImageJ Segmented Line tool). A linearity value 1 represents a straight line.

Calculation of initial recoil velocity after ablation

The length of ablated cell boundary was measured overtime by using ImageJ Straight Line tool. Data points before the cut were fit with linear line. An exponential was used to fit the data after the cut. The effective time of the cut was found as the intersection of the linear line with the exponential. The initial recoil velocity was found from the deliberative of the exponential at effective time of the cut. The velocity was calculated in Matlab. More detail can be found in (Hara et al., 2016).

Quantitative analyses of the deformation in the shape of extruding LECs

To quantify the local/isotropic deformation of extruding LEC, as shown in Fig. 1e (before τ_{area}) and 1e' (after τ_{area}), we first measured the differences in cell shapes at two different time points (Fig. S4a). Before τ_{area}, the differences in cell shapes at [τ_{area}-25] min and τ_{area} min was shown as gray area in Fig. S4a (left). The centoid of this gray area (residual area) and the cell area at τ_{area} (white area) were shown as a red and black cross, respectively. We then defined the black cross as the origin of the new coordinate system. We further rotated the coordinate so that y-axis represented the direction toward histoblast. After τ_{area}, the differences in cell shapes at τ_{area} min and [τ_{area}+25] min was shown as gray area in Fig. S4a (right). The centoid of this gray area (residual area) and the cell area at [τ_{area}+25] (white area) were shown as a blue and black cross, respectively. Finally, we analyzed 6 cells before and after τ_{area}, and summarized all data in a same graph (Fig. S4b).

Statistics

All the p values are calculated using a student t-test: $p < 0.05$, significantly different; $p > 0.05$, not significantly different.

Development • Supplementary information

Supplemental References

Aigouy, B., Farhadifar, R., Staple, D.B., Sagner, A., Roper, J.C., Julicher, F. & Eaton, S. (2010). Cell flow reorients the axis of planar polarity in the wing epithelium of Drosophila. *Cell,* 142**,** 773-86.

Hara, Y., Shagirov, M. & Toyama, Y. (2016). Cell Boundary Elongation by Non-autonomous Contractility in Cell Oscillation. *Current biology : CB,* 26**,** 2388-96.

Huang, J., Zhou, W., Dong, W., Watson, A.M. & Hong, Y. (2009). Directed, efficient, and versatile modifications of the Drosophila genome by genomic engineering. *Proceedings of the National Academy of Sciences,* 106**,** 8284-8289.

Nakajima, Y.-I., Kuranaga, E., Sugimura, K., Miyawaki, A. & Miura, M. (2011). Nonautonomous Apoptosis Is Triggered by Local Cell Cycle Progression during Epithelial Replacement in Drosophila. *Molecular and Cellular Biology,* 31**,** 2499-2512.

Ninov, N. & Martin-Blanco, E. (2007). Live imaging of epidermal morphogenesis during the development of the adult abdominal epidermis of Drosophila. *Nature Protocols,* 2**,** 3074-3080.

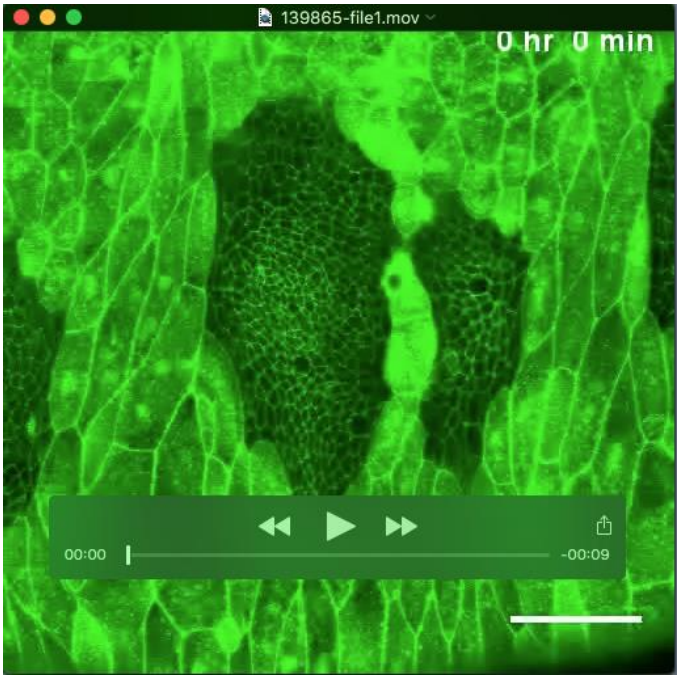
Schneider, C.A., Rasband, W.S. & Eliceiri, K.W. (2012). NIH Image to ImageJ: 25 years of image analysis. *Nature methods,* 9**,** 671-5.

Takemoto, K., Nagai, T., Miyawaki, A. & Miura, M. (2003). Spatio-temporal activation of caspase revealed by indicator that is insensitive to environmental effects. *The Journal of cell biology,* 160**,** 235-43.

Wang, W. & Yoder, J.H. (2011). Drosophila pupal abdomen immunohistochemistry. *J Vis Exp*.

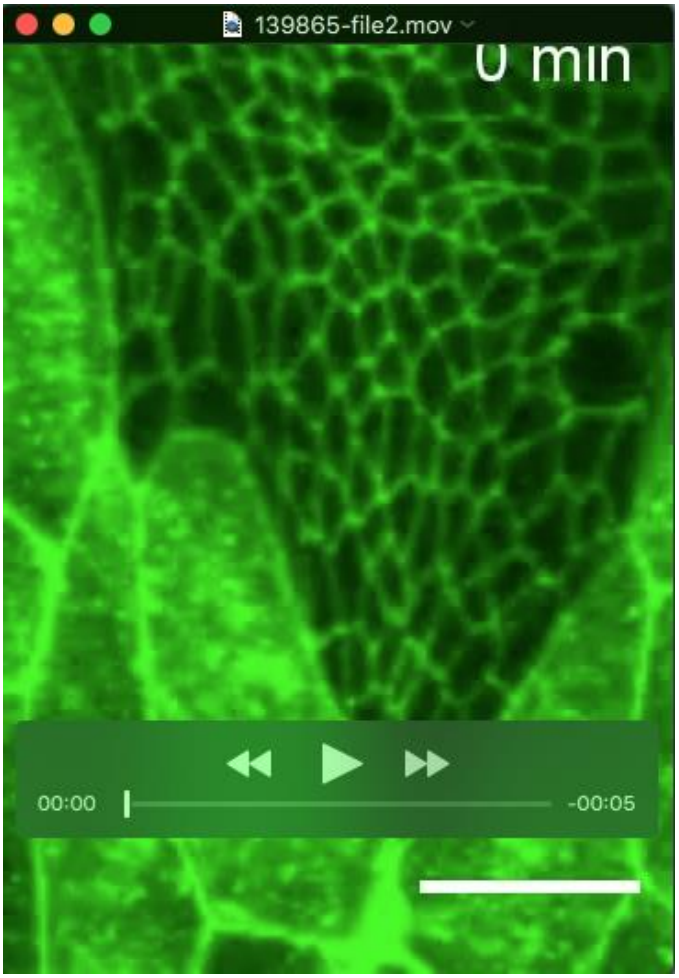
Development • Supplementary information

Supplemental Movies



Movie 1. Time-lapse images of wild-type pupa expressing *ubi-D*E-cad::GFP. Scale bar, 50 µm.

Development • Supplementary information



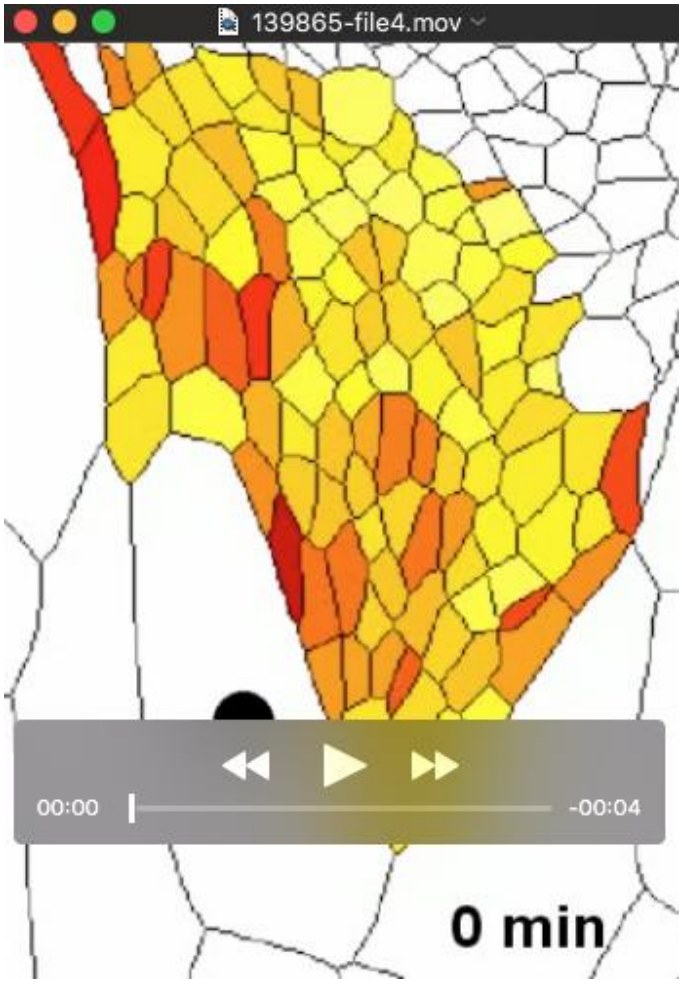
Movie 2. Time-lapse images of wild-type pupa expressing *ubi-D*E-cad::GFP. Scale bar, 20 µm.

Development • Supplementary information



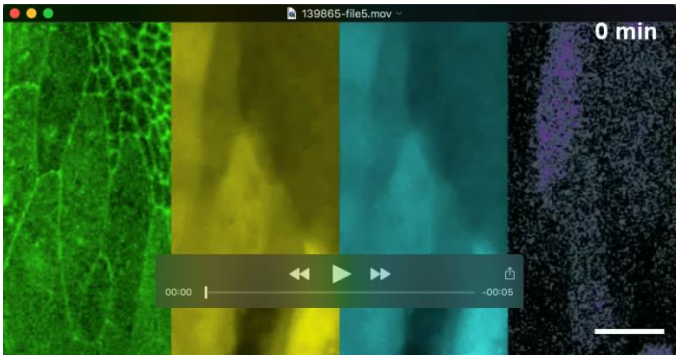
Movie 3. Time-lapse images of wild-type pupa expressing Lifeact::GFP. Top view and orthogonal views. Scale bar, 20 µm.

Development • Supplementary information



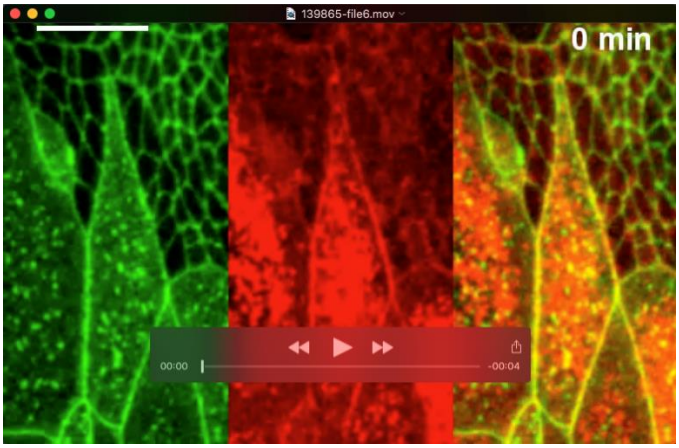
Movie 4. Color-enhanced reproduction of the confocal images from Movie 3. Colors demote the anisotropy of cell shape (as illustrated by the color bar in Fig. 1c).

Development • Supplementary information



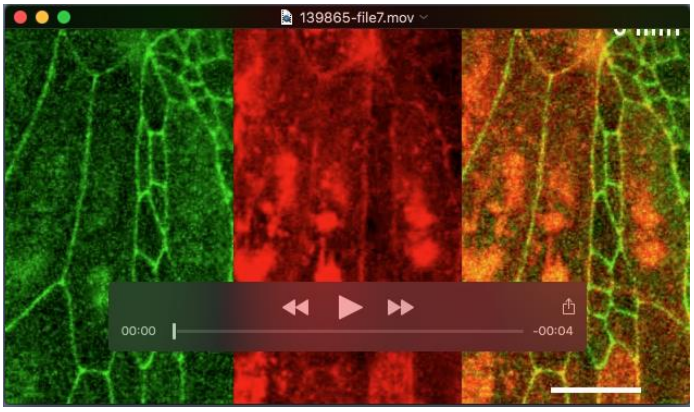
Movie 5. Time-lapse images of wild-type pupa expressing *D*E-cad::mTomato^{KI} (green), FRET-base caspase-3 sensor SCAT3 (Venus: yellow, ECFP: cyan), and FRET ratio (perple - white). Scale bar, 20 μm.

Development • Supplementary information



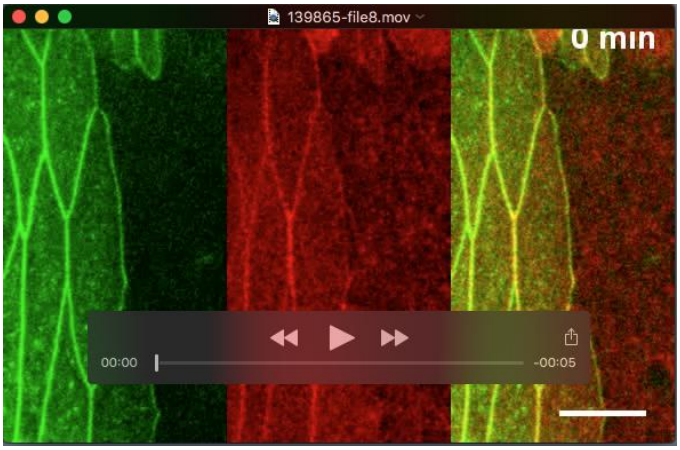
Movie 6. Time-lapse images of of wild-type pupa expressing *ubi-D*E-cad::GFP (green) and MyoII::Cherry (red). Scale bar, 20 μm.

Development • Supplementary information



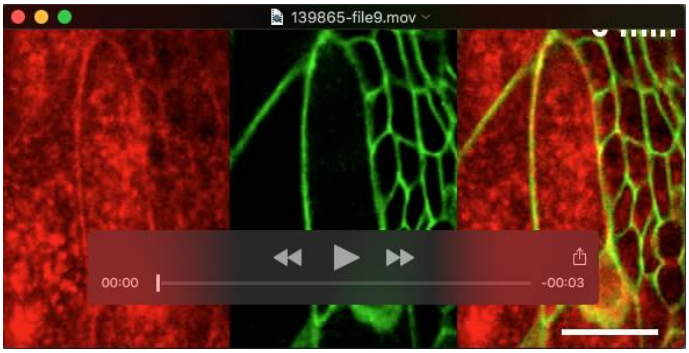
Movie 7. Time-lapse images of wild-type pupa expressing β-cat::YFP (green) and MyoII::Cherry (red). Scale bar, 20 μm.

Development • Supplementary information



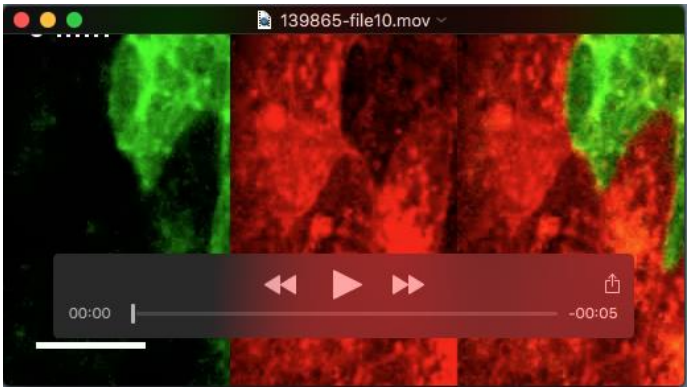
Movie 8. Time-lapse images of wild-type pupa expressing α-cat::RFP (green) and MyoII::GFP (red). Scale bar, 20 μm.

Development • Supplementary information



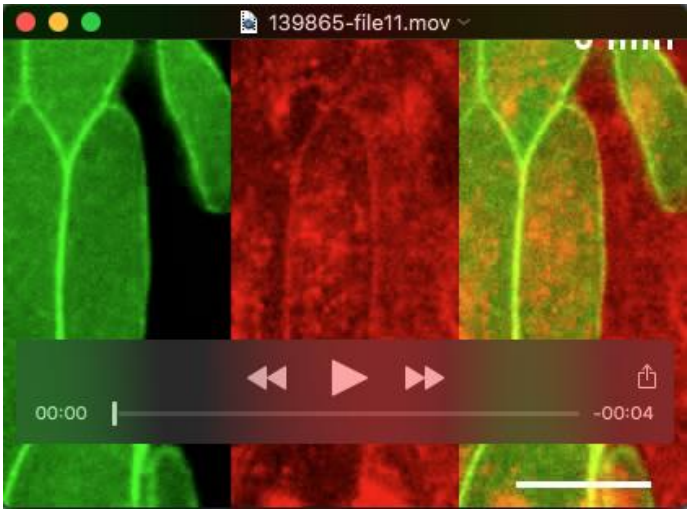
Movie 9. Time-lapse images of wild-type pupa expressing Nrg::GFP (green) and MyoII::Cherry (red). Scale bars, 20 μm.

Development • Supplementary information



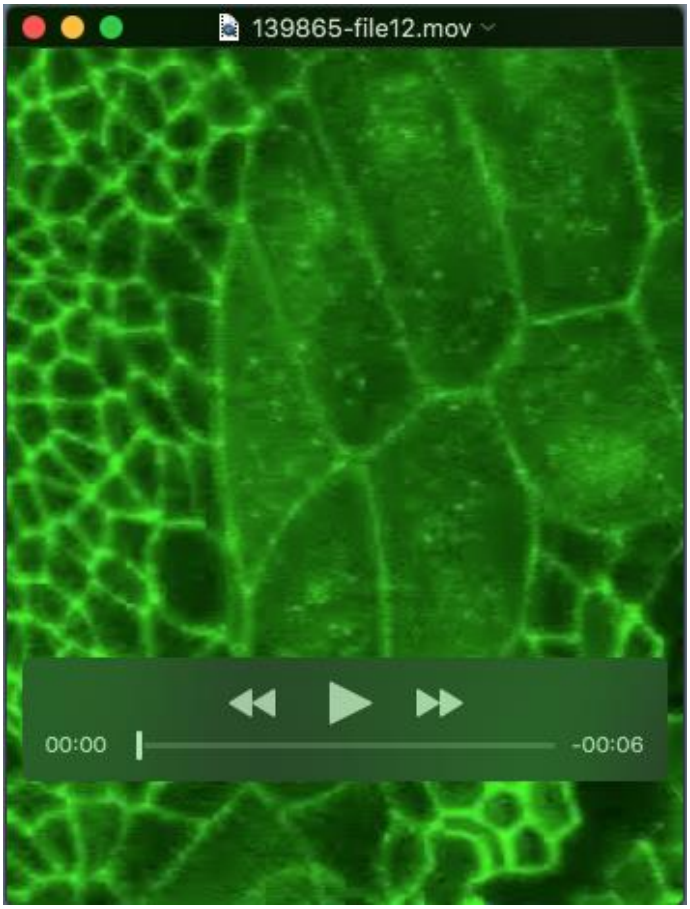
Movie 10. Time-lapse images of wild-type pupa expressing MyoII::GFP in histoblasts (green) and MyoII::Cherry (red) ubiquitously. Scale bar, 20 μm.

Development • Supplementary information



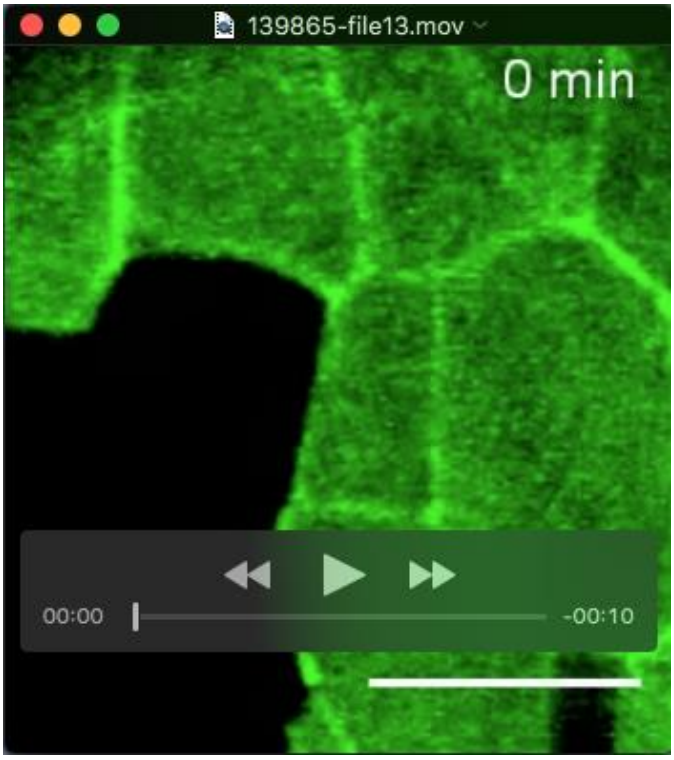
Movie 11. Time-lapse images of wild-type pupa expressing MyoII::GFP in LECs (green) and MyoII::Cherry (red) ubiquitously. Scale bar, 20 µm.

Development • Supplementary information



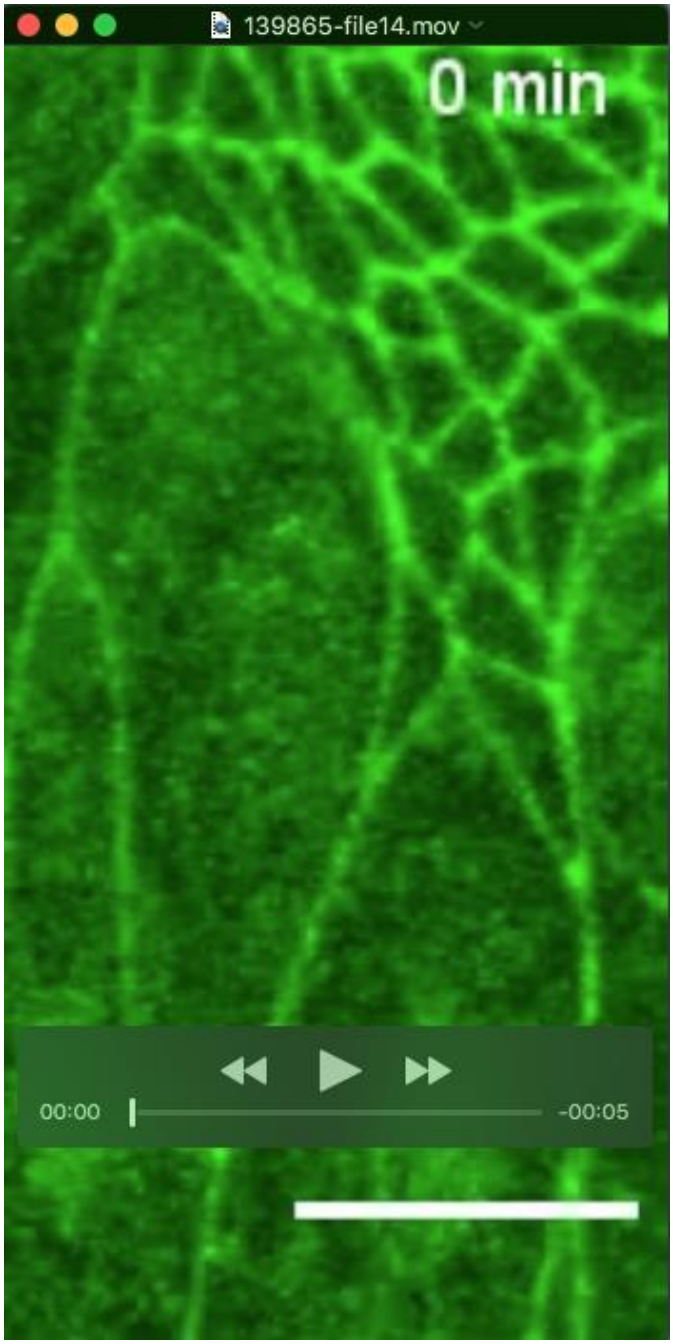
Movie 12. Time-lapse images of pupa expressing caspase inhibitor p35 only in LECs and expressing E-cad::GFP^{KI} (green) ubiquitously. Scale bar, 20 µm.

Development • Supplementary information



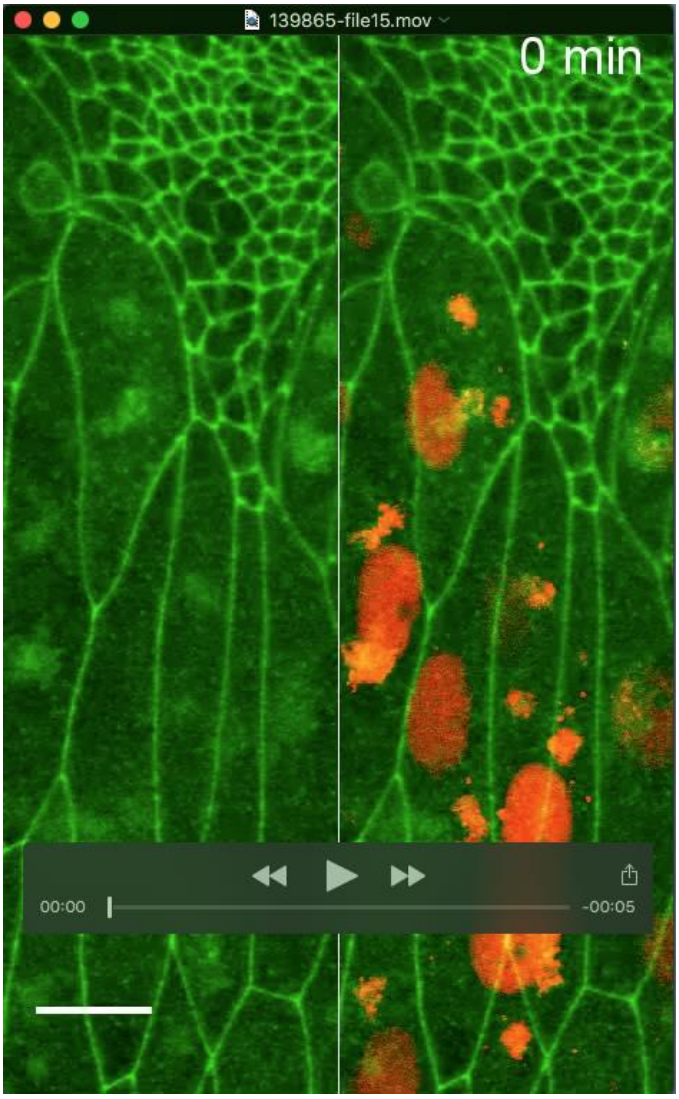
Movie 13. Time-lapse images of pupa expressing caspase inhibitor p35 and MyoII::GFP (green) only in LECs. Scale bar, 20 μm.

Development • Supplementary information



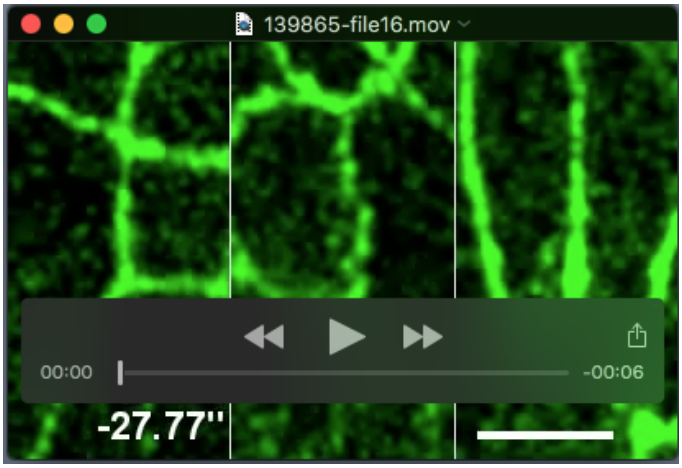
Movie 14. Time-lapse images of pupa expressing sqh-RNAi only in LECs and expressing E-cad::GFP^{KI} (green) ubiquitously. Scale bar, 20 μm.

Development • Supplementary information



Movie 15. Time-lapse images of pupa with clonal expression of *sqh*-RNAi. E-cadherin::GFP (green) and Histone::Cherry (red). Scale bar, 20 μm.

Development • Supplementary information



Movie 16. Time-lapse images of laser ablation on pupa with *D*E-cad::GFP. The ablations were performed in three different stage of apoptotic cell extrusion: before the reduction of E-cad (left); right after the reduction of E-cad (middle); and during the contraction of actomyosin cable in the neighboring cells (right). Scale bar, 5 μm.

Development • Supplementary information